Alkali-activated grouts based on slag-fly ash mixtures: From early-age characterization to long-term phase composition

Abdelilah Aboulayt, Faten Souayfan, Emmanuel Rozière, Reda Jaafri, Anass Cherki El Idrissi, Redouane Moussa, Christophe Justino, Ahmed Loukili

Alkali-activated grouts based on slag-fly ash mixtures: from early-age characterization to long-term phase composition

Abdelilah Aboulayt[a,b], Faten Souayfan[a], Emmanuel Roziere[a *], Reda Jaafri[a], Anass Cherki El Idrissi[a] , Redouane Moussa[c], Christophe Justino[d], Ahmed Loukili[a]

[a] Civil engineering and Mechanics Research Institute (GeM), UMR-CNRS 6183, Ecole Centrale de Nantes, 1 rue de la Noe, 44321 Nantes, France.

[b] Materials Science, Energy and Nano-engineering Department, Mohammed VI Polytechnic University, 43150 Ben Guerir, Morocco.

[c] University Hassan II Casablanca, Faculty of Sciences Aïn Chock, Laboratory of Physical Chemistry of Inorganic Materials, Casablanca, Morocco.

[d] Soletanche-Bachy, Chemin des Processions – 77130 Montereau Fault Yonne, France.

* Corresponding author: Emmanuel.Roziere@ec-nantes.fr

Abstract

Alkali-activation and the combination of slag and fly ash are expected to improve the chemical stability of grouts designed for underground works. Sodium silicate activated grout mixtures have been designed with a liquid activator volume fraction of 75%. As the data related to such high water-to-solid ratios are scarce, a comprehensive study has been designed in order to determine the phase composition of these grouts and thus understand the influence of fly ash proportion on engineering properties of grouts at both fresh and hardened states. The reactivity at early-age is mainly provided by slag with a drop in strength from 60% of fly ash. Nuclear magnetic resonance (NMR), X-ray diffraction (XRD), and Fourier transform infrared spectroscopy (FTIR) have been used to investigate the phase assemblage at long term (700 days). The alkali-activation of slag mainly produces a calcium silicate hydrate substituted with aluminum (C-A-S-H). From 20% of fly ash the C-A-S-H phase coexists with sodium aluminosilicate gel N-A-S-H, predominant from 60% of fly ash.

Keywords: grouts, alkali-activated binder, fly ash, ground granulated blast-furnace slag, NMR, phase composition.

1. Introduction

Deep soil-mixing consists in mixing the existing soil with a grout to improve its physical and mechanical properties. The method does not involve any compaction and therefore grouts generally have high wet fractions to achieve the necessary fluidity to obtain a homogeneous and uniform binder-soil mixture throughout the injection depth. The operating techniques require the elaboration of sufficient quantity of grouts which must be stable against bleeding during storage and before injection. From the structural point of view, the grout mixture is designed to provide the soil-grout composite material with adequate mechanical properties and durability in actual exposure conditions. These goals are usually attained and controlled by rheological testing, the monitoring of mechanical properties and chemical analyses. It should be noted that the addition of various chemical admixtures may also modify grouts properties after setting, although they are generally intended to improve first of all the rheological properties of the grout at fresh state. In order to avoid bleeding, several solutions can be envisaged, either by acting on the solid fractions, by the addition of natural or synthetic solids like bentonite or by acting on the liquid fraction by means of viscosity modifiers additions (stabilizing agents) [1,2]. Viscosity-Enhancing admixtures are water-soluble polymers, that include a natural polysaccharide-based polymer called xanthan gum, which is widely used to modify the viscosity of cement based materials [3,4]. Technically, several methods deal with the testing and measurement of properties at fresh state, namely: rheometry, mini-slump and Marsh cone test. The Marsh cone test is widely adopted as a workability test for the specification of cement-based grouts. It is commonly used for the quality control for injection purposes, thanks to its easy measurement compared to laboratory rheological tests [5–7].

Besides plain and blended cement-based materials, alkali activated materials (AAM) including metakaolin based geopolymers are also considered for soil improvement [8,9].

Additionally, AAM can be designed from byproducts of several industries, for instance ground granulated blast furnace slag (GGBFS) and fly ash (FA), due to their relatively low cost and composition [10].

The activation of slag by alkali-based and cement-based activating solutions generally provides the fresh and hardened materials with good engineering properties, even if the setting and hardening kinetics of some alkali-activated mixtures is still an issue [11]. The reactivity and the microstructure of activated slag mixtures have been widely studied and their main features are now rather well-known [12–14]. The reaction products mainly consist in calcium silicate hydrates substituted with aluminum (C-A-S-H) favored by the relatively high calcium content. Alkali-activated fly ash has already been used for deep soft soil improvement [15], but the authors observed a relatively slow development of strength [16]. Even if this type of material finally reached higher strength than cement-based material used in the same conditions, segregation was observed, and 3-month strength was only 40 to 60% of 1-year strength. The interest in such low-calcium alkali-activated materials remains high as they are expected to provide better chemical and physical stability in severe exposure conditions. Their microstructure has actually been shown to differ significantly from high-calcium systems such as cement and slag. Reduced calcium and significant aluminum contents promote the formation of a highly polymerized aluminosilicate phase N-A-S-H [17].

Binary slag-fly ash mixtures are thus expected to combine the interests of slag-based and fly-ash based compositions in terms of the early age as well as the hardened state properties. For example, the easy dissolution of alumino-silicates from slag promotes the rapid setting and increases the strength while adding fly ash was found to delay setting, which could be exploited to control the setting time and hardening of the blend at the early age [18]. Varying the proportions of both precursors represents another parameter to meet the specifications for fresh state, short-term and long-term behaviors. The partial replacement of fly ash by slag

leads also to the improvement on the resistance to acids [19]. The publications related to these binary mixtures are still relatively scarce [20–23]. Most of published studies have dealt with compositions of relatively high dry fraction whereas grout mixtures are generally designed with significantly higher water-to-solid ratios. Due to the different reactivity of slag and fly ash, the microstructure of slag-fly ash mixtures strongly depends on curing time. This results in complex interactions between forming phases. C-A-S-H and N-A-S-H gels can coexist, as shown by studies were performed on synthetic materials [24,25], hybrid cements based on fly ash, and other binders. N-A-S-H resulting from the reaction of fly ash tend to evolve into (N,C)-A-S-H in the presence of calcium, however a part of N-A-S-H gel may remain depending on the calcium content on the mixture. The proportion of the reaction products was also found to depend on the alkalinity [26,27]. The existence of a hybrid sodium and aluminum substituted calcium silicate hydrate C-N-A-S-H has also been suggested [22]. Ismail et al. [22] studied samples with a relatively low water-to-binder ratio of 0.40. From a 25% of fly ash they observed the formation of two distinct gels, C-A-S-H and N-A-S-H-type. From 50% a hybrid phase (N,C)-A-S-H gel was identified, and from 75% of fly ash C-A-S-H content was negligible. Their diagram was based on EDX, which does not fully describe the structure of the so-called hybrid phase. EDX actually provides the proportion of elements but not the atomic bonding and environment of elements. Other studies did not include NMR [18,21] although investigating the environments of aluminum and silicon through this technique allows a deeper investigation of the phase assemblage of alkali-activation products. This phase composition can then be used to understand the evolution of engineering properties. Several studies focused on the microstructure and phase assemblage [20,28], thus they do not allow understanding the influence of initial composition on macroscopic properties [29]. The engineering properties and long-term phase composition of fly ash-slag

grouts with high water-to-solid ratio are still not well known, hence the need for a comprehensive study based on relevant experimental techniques.

This work is a part of a testing program aimed at designing and studying diluted grouts from different raw materials in order to optimize the mix-design of grouts to be used for deep soil-mixing. The durability of grouts was not in the scope of the study. Previous studies have shown the influence of chemical composition and phase assemblage on the resistance to aggressive waters. For instance the CaO content was found to influence the organic acid resistance of alkali-activated binders [30]; geopolymers showed better durability in strongly acid solutions [31], hence the need for studying the long-term phase assemblage of a wide range of compositions. The engineering properties include the properties at fresh and hardened states [1,2,16]. Fly ash and slag proportions have been varied from 0 to 100% keeping the composition and the proportion of the sodium silicate activating solution constant. A preliminary study allowed determining the minimum content of organic stabilizer necessary to avoid bleeding of the grout for a given proportion of FA. The short-term characterization includes Marsh cone, isothermal calorimetry, compressive strength, and scanning electron microscopy (SEM). The investigation on phase composition requires experimental techniques giving access to the molecular structure. The magic angle spinning nuclear magnetic resonance (MAS NMR) has been reported to be a useful tool to study aluminosilicates [28]. The composition of hardened grouts at long-term has also been investigated using X-ray diffraction (XRD), and Fourier transform infrared spectroscopy (FTIR).

2. Materials and methods

2.1 Materials

Two types of raw materials are required to design the studied grouts, namely: precursors and liquid activator (Table 1). The dry fraction is composed of ground granulated blast furnace slag (GGBFS) from Fos, France and fly ash (FA) from Hornaing, France. The liquid fraction,

129 which will be called activation solution, consists of sodium hydroxide mixed with a
130 commercially available sodium silicate solution (Table 1). Silicate solution used in this study
131 provides a SiO_2/Na_2O molar ratio (modulus) of 1.7 and 44wt% of dry matter. It is noteworthy
132 that this molar ratio is relatively low. The sodium silicate solution used in this study has been
133 especially designed by the provider with higher initial Na_2O content to minimize NaOH adding
134 during the preparation of grouts, as the dissolution of NaOH can be a hazardous operation. The
135 liquid activator was actually prepared by mixing the sodium silicate solution with a 0.2 M
136 NaOH solution. Commercial sodium silicate solution generally have a modulus around 3. The
137 activator used in this study is equivalent to a sodium silicate solution of modulus of 3 mixed
138 with a 3.9 M NaOH solution. As needed, an appropriate amount of stabilizing agent is added
139 during mixing (Table 3).

140 The particle size distributions of dry powders were obtained using submicron NICOMP 380
141 granulometer with distilled water as a dispersant. Interactions between analyzed powders and
142 water were possible but these were not expected to affect their properties due to short testing
143 time. The specific surface area (SSA) was determined through an analysis from Brunauer,
144 Emmett and Teller (BET) theory.

145

146 Table 1. Raw materials.

Component	Content, *Commercial name*	Density (g/l)
Water	Demineralized water	1000
NaOH	Sodium hydroxide pellets *Sigma Aldrich*	1460
Sodium silicate	Sodium silicate solution, *Geosil*	1550
Stabilizing agent	Xanthan gum-based admixture *Betolin V30*	750
GGBFS	Ground granulated blast furnace slag, *Ecocem*	2900
Fly Ash	Fly ash powder, *Silicoline*	2240

GGBFS and FA have d_{10}, d_{50} and d_{90} diameters of respectively 2 µm, 11 µm and 30 µm, and 6 µm, 39 µm and 175 µm. They reflect a fine distribution for both powders. The specific areas are 0.45 m^2/g for GGBFS and 1.24 m^2/g for FA. Such fine particles are suitable to improve the reactivity of precursors and ensure then good early-age reactivity.

The chemical compositions, obtained from XRF analysis, are presented in Table 2. GGBFS mainly consists of silica (37.2 wt.%), alumina (10.5 wt.%), and a significant proportion of CaO (43.2 wt.%). The fly ash was characterized by a silica content of 50 wt.%, an alumina content of 20 wt.%, and a high proportion of iron oxide (8.5 wt.%).

Table 2. Quantitative chemical composition of powders (wt.%) and properties of powders.

	SiO_2	Al_2O_3	CaO	Fe_2O_3	MgO	SO_3	Cl	TiO_2	Na_2O	Median Diameter (µm)	Density (g/cm^3)	BET (m^2/g)	Packing density (vol. %)
GGBFS	37.2	10.5	43.2	0.6	7	0.1	0.01	0.5	0.6	10	2.89	0.45	44.4
Fly ash	50	20	1	8.5	3	0.6	0.04	1	0.6	38	2.24	1.24	62.6

X-ray diffraction patterns of dry materials precursors used in this study are shown in Figure 1. The diffractogram of fly ash shows the characteristic peaks of quartz (SiO_2, PDF # 01-083-2466), mullite ($Al_{2.4}Si_{0.6}O_{4.8}$ PDF# 01-073-1389) and iron oxide (maghemite) (Fe_2O_3, PDF# 01-089-5892) as major crystalline phases. These peaks are overlapped with a hump at (15°-38°) 2θ range that corresponds to an amorphous fraction. GGBFS is mainly composed by amorphous phases, as only an isolated hump can be observed at (20°-38°) 2θ range.

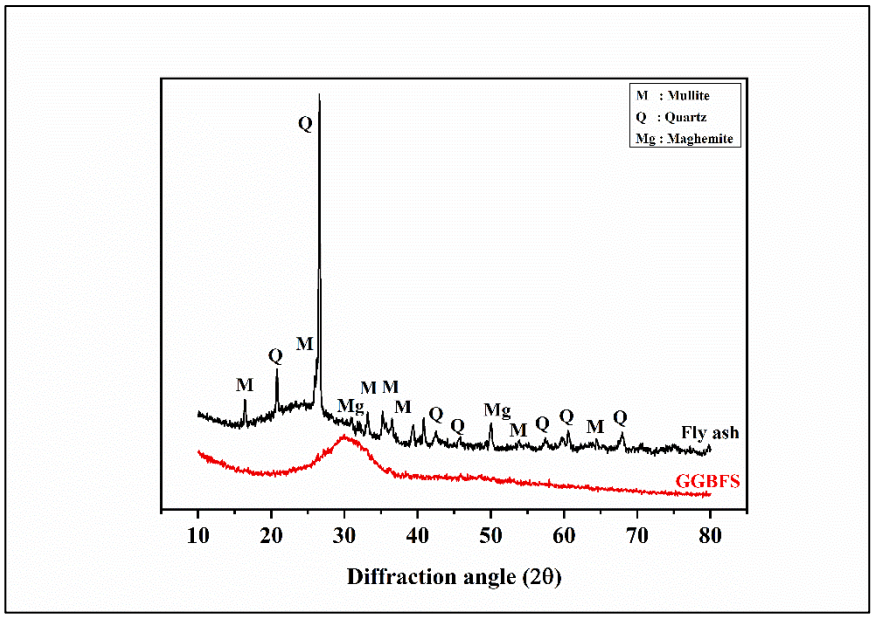

166

167 Figure 1. XRD pattern of fly ash and ground granulated blast furnace slag.

168

169 It can be concluded from the physical properties and mineralogy of raw powders that they can
170 represent good candidates for the alkali-activation.

171

172 **2.2 Mixture compositions and sample preparation**

173 The specifications on grouts generally include performances at the fresh and hardened states.
174 This study was aimed at providing relevant data for designing fluid but stable grouts with good
175 mechanical performances and elaborated with relatively low-carbon raw materials. Given their
176 intended use i.e. a technique of deep soil-mixing, the grouts are sought to ensure low viscosity
177 in terms of Marsh flow time, low bleeding within 24 hours (< 5%), and a compressive strength
178 higher than 5 MPa at 28 days.

179 In order to design an optimized and stable binary mixture incorporating fly ash, it was first
180 necessary to determine the influence of solid fraction. Bleeding decreased with the volume
181 fraction of powders. The same finding was also indicated in a similar work [2]. Therefore, a

182 water-to-solid ratio of the order of 0.70 was found to give a good compromise between
183 stability and fluidity in accordance with the operating specifications indicated above. This ratio
184 is considered as a basis for choosing the dry matter proportions of this study. The design of
185 optimized slag-fly ash binary mixtures was derived from a stable 100 wt.% grout of GGBFS.
186 GGBFS was replaced by increasing proportions of FA up to 100 wt.%. The total volume of
187 powders (GGBFS and FA) was kept constant at 25% of the volume of the mixture; the volume
188 fraction of the liquid activator was 75%. As the bleeding tends to increase with slag
189 replacement, different amounts of xanthan gum (0, 0.2, 0.4 and 0.6% of activator) were added
190 as a stabilizer.

191 A 0.2M NaOH solution is prepared by adding chemical grade NaOH pellets in demineralized
192 water. This solution is mixed with the sodium silicate solution, then the stabilizer is added. As
193 indicated in the product specifications, this is stable towards acids and alkalis. After the
194 preparation of the activating solution, dry materials were added. Different mixtures with
195 variable stabilizer contents have been prepared, in order to select stable mixtures (Table 3).
196 Only stable mixtures were fully characterized as indicated in section 2.3.

197 Table 4 gives the corresponding theoretical molar ratios of the studied mixtures. The values of
198 limit 1 were calculated without taking into account the dissolution of fly ash. The limit 2
199 corresponds to full dissolution of fly ash. This second limit is theoretical as the fly ash contains
200 crystalline phases that cannot be dissolved even after significant reaction time. The actual
201 behavior of the studied mixtures is expected to figure between these two limits. These two
202 assumptions are used to discuss the influence of the generally slower reactivity of fly ash in
203 alkali-activated mixtures (section 3).

204

205

206 Table 3. Compositions of studied mixtures.

Designation	Powder proportions		Dry materials		Activating solution			Water / Solid
	GGBFS (wt. %)	**FA** (wt. %)	**GGBFS** (g)	**FA** (g)	**Sodium silicate** (g)	**NaOH (0.2 mol/l)** (g)	**Stabilizer** (wt. %)	
G100FA00	100	0	740	0	583	370	**0**	0.70
G80FA20	80	20	592	114	583	370	**0.2**	0.72
G60FA40	60	40	444	229	583	370	**0.4**	0.75
G40FA60	40	60	296	343	583	370	**0.6**	0.78
G20FA80	20	80	148	457	583	370	**0.6**	0.81
G00FA100	0	100	00	571	583	370	**0.8**	0.84

207

208 Table 4. $SiO_2 – Al_2O_3 – CaO$ diagram of studied mixtures

	Studied mixtures (molar ratios)			$SiO_2 – Al_2O_3 – CaO$ diagram					
				Limit 1: No dissolution of FA			**Limit 2: Full dissolution of FA**		
	Ca/(Al+Si)	**Al/Si**	**Na/Al**	**SiO_2**	**Al_2O_3**	**CaO**	**SiO_2**	**Al_2O_3**	**CaO**
G100FA00	0.71	0.21	4.4	53	6	42	53	6	42
G80FA20	0.57	0.23	4.0	55	5	40	57	7	36
G60FA40	0.42	0.25	3.7	58	5	37	63	8	30
G40FA60	0.28	0.27	3.4	63	4	32	69	9	22
G20FA80	0.14	0.28	3.2	73	3	23	76	11	13
G00FA100	0.01	0.30	3	100	0	0	86	13	1

209

210 **2.3 Experimental techniques**

211 Several techniques have been implemented in the experimental program considered in this
212 investigation. This program combines analyses to characterize the raw materials, to monitor
213 the evolution of the reaction products during the hardening stage as well as to evaluate the
214 phase composition of the hardened grouts at longer term. This comprehensive study was meant
215 to investigate the influence of the chemical and microstructural changes on the development of

engineering properties, such as compressive strength. Isothermal calorimetry provides the time evolution of chemical reactivity; XRD, FTIR, and NMR allow identifying the reaction products at long-term. The microstructure was directly observed with scanning electron microscopy (SEM). During the first 28 days, the evolutions of heat release, strength, and microstructure can thus be compared. Table 5 summarizes the ages of grout samples for each characterization method used during this study. The FTIR and NMR characterizations of slag and fly ash are given as supplementary materials (Appendix A).

Table 5. Investigated properties: nature, characterization method and samples age.

Nature	Characterization method	Age of samples
Fresh state and hardening	Bleeding	During the first 24 hours
	Isothermal calorimetry	During the first 7 days
Hardened early age properties	Mechanical properties	7 days and 28 days
	SEM observations	28 days
Mineralogical and nanostructural study in hardened long-term systems	XRD	700 days
	FTIR	
	^{29}Si and ^{27}A1 NMR MAS	

2.2.1 Marsh cone

Flow time was obtained from Marsh cone according to standard EN 445. In terms of engineering properties, the mix-design is expected to minimize bleeding, Marsh flow time, and heat release. Mash cone is often used to characterize the viscosity of grouts although the flow time does not only depend on this rheological parameter [32].

235 2.2.2 Bleeding test

236 The aim of bleeding tests is to characterize the stability of the grout. The bleeding rate (ΔH_{24})
237 is evaluated by measuring the distance between the separation of liquid and solid fractions and
238 the top of the tube (H_0) (Figure 2).

239

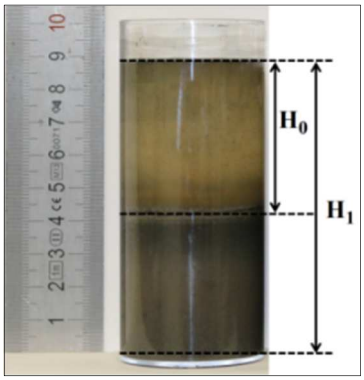

240

241 Figure 2. 24h bleeding of 100 wt.% fly ash grout.

242 The suspensions are placed in a bleeding test tube (transparent cylinder of height H_1 =9 cm
243 and 4cm diameter) and left to rest for 24 hours. Bleeding is calculated according to the
244 equation (1) [2]. Only stable mixtures corresponding to zero-bleeding were fully characterized
245 thereafter.

246 $$\Delta H_{24} = \frac{H_0}{H_1} \times 100 \quad (1)$$

247

248 2.2.3 Isothermal calorimetry

249 The reactivity of studied mixtures at early age is investigated by monitoring the heat flow
250 (dQ/dt), released during the reaction, from the end of mixing for the first 7 days. Fresh grouts
251 are mixed and poured into ampoules, sealed then immediately placed in a TAM AIR
252 isothermal calorimeter at a temperature of 20 °C. The cumulative heat was deduced by the
253 integration of the measured flux. By plotting the cumulated heat as a function of 1/√t, a linear

254 evolution is obtained for small values of $(1/\sqrt{t}\ )$ as shown in Figure 3. This allows
255 determining the ultimate value of released heat, as the intersection with Y-axis, then the value
256 at 28 days.

257
258

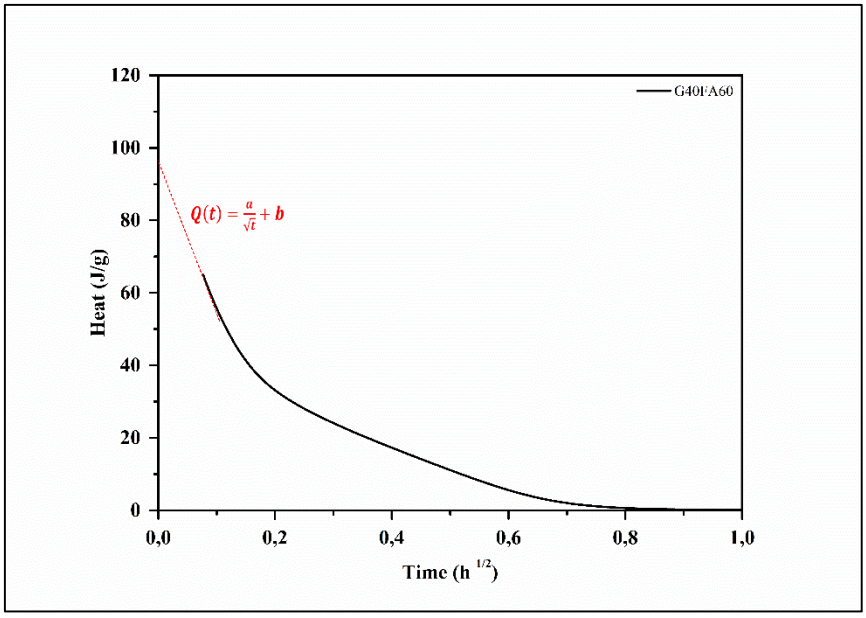

259

260 Figure 3. Heat extrapolation method on G40FA60 data.

261

262 2.2.4 Compression tests

263 Compression tests on 4x4x4 cm^3 cubic samples provided the strength of the hardened grouts
264 cured at 20 °C in sealed conditions and then tested at 7 and 28 days. These tests were
265 performed on a universal testing machine at a loading rate of 1 kN/s.

266

267 2.2.5 Scanning electron microscopy

268 JEOL type scanning electron microscope (SEM) was used for the observation of polished
269 specimen surfaces under partial vacuum. The pressure in the specimen chamber was 50 Pa
270 and the accelerating voltage was 20 kV.

271

272 2.2.6 X-ray diffraction and FTIR

273 Mineralogical analysis of raw powders and hardened grouts was conducted using X-ray
274 diffraction (Bruker AXSD4, Cu Ka = 0.154 nm) and Fourier transform infrared spectroscopy
275 (FTIR) whose spectra were collected, using a Shimadzu spectrometer, in transmittance mode
276 from 400 to 4000 cm^{-1} using standard KBr technique. Spectra were normalized with correction
277 of the baselines without any influence on the positions, widths or intensities of the bands.

278 2.2.6 Nuclear magnetic resonance spectroscopy

279 If XRD is mainly used for characterizing crystalline structures, nuclear magnetic resonance
280 spectroscopy (NMR) combined with FTIR are considered as an appropriate technique for
281 studying the bonding and environment of elements thus the phase composition of amorphous
282 and semi-crystalline alumino-silicates of high heterogeneity. For NMR spectroscopy, 80 mg
283 of grounded specimens were packed into 4 mm zirconia rotors. ^{29}Si and the $^{27}A1$magic-angle
284 spinning nuclear magnetic resonance (MAS NMR) were acquired using a 6000 MHz Bruker
285 Advance III spectrometer with operating frequencies of 119 MHz. For ^{29}Si the rotor spun at 8
286 kHz with an excitation pulse of 3.5μs and a recycle time of 15 s. For $^{27}A1$, the rotor spun at 10
287 kHz with an excitation pulse of 1.8μs and a recycle time of 5 s. Spectra were referenced
288 against Tris(trimethylsilyl)silane; ($[(CH_3)_3Si]_3SiH$) for ^{29}Si and $Al(NO_3)_3$ for ^{27}Al. Gaussian
289 line model was used for deconvolution of ^{29}Si MAS NMR spectra. As recommended by
290 several recent studies, the minimum possible of peaks were fitted by considering the full
291 width at half height (FWHH) constant [33,34]. Peak positions and widths were kept constant
292 throughout all spectral deconvolutions, peak locations are based on the available literature
293 [14,34–36].

294

295

296

3. Result and discussions

3.1 Properties of fresh grouts

Figure 4 shows the influence of stabilizer content and FA proportion on bleeding. Bleeding increased with FA proportion, but relatively low admixture contents (up to 0.6% of the activator) allowed mitigating bleeding, excepted for FA100 mixture.

Higher replacement of slag by fly ash lead to higher stabilizer content needed for reaching zero bleeding (Table 3). Only stable mixtures were fully characterized. It should be noted that 100 wt.% FA mixture did not develop significant mechanical properties during the first 28 days; therefore it will not be considered in this work. Stabilized compositions, associated to the required stabilizer amount, are described in Table 3. They were subjected to several characterization methods, at both the fresh and the hardened state.

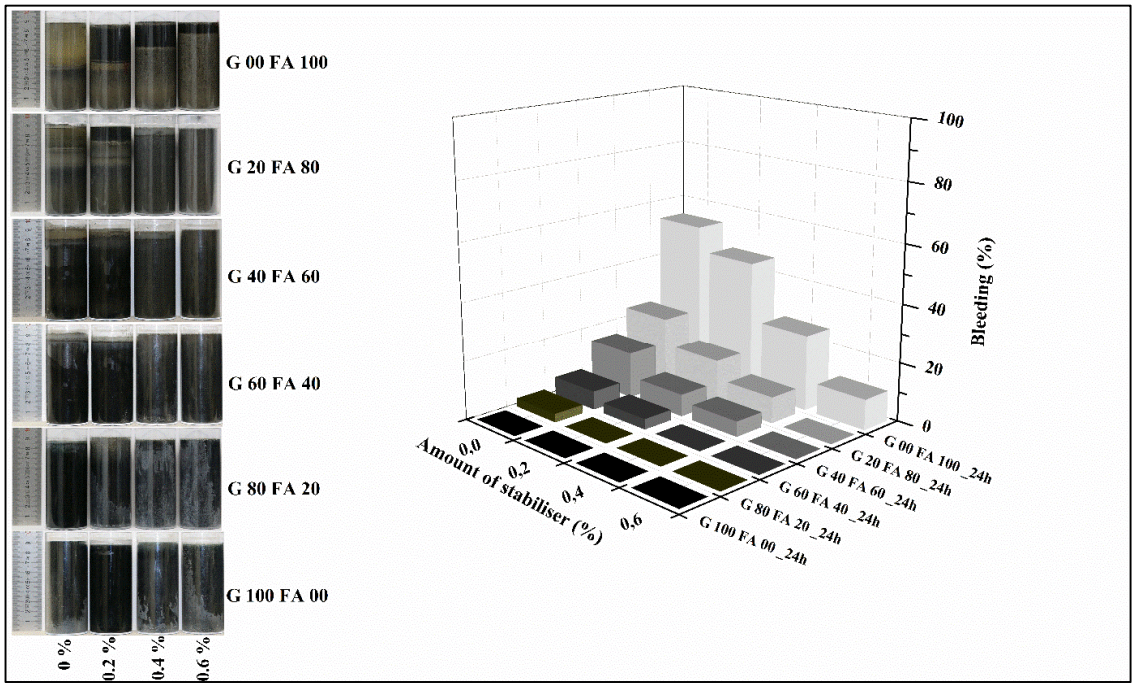

Figure 4. Bleeding after 24 hours versus GGBFS content and stabilizer amount.

312 The Marsh flow time also increased with xanthan gum content (Table 6).-Only G100FA00 and
313 G80FA20 mixtures showed values lower than 2 minutes [2], which is generally recommended
314 for the process. The increase in flow time could be explained by higher viscosity of the
315 activating solution. In a previous study, the rheological characterization of the same activating
316 solution revealed that the viscosity significantly increases with the increase of the amount of
317 xanthan gum [2]. The stabilizer also induces an increase in the yield stress of the solution,
318 which prevents the decantation of solid particles.
319

320 Table 6. Marsh flow time of stabilized grouts.

Mixtures	Marsh flow time (min)
G 100 FA 00	1.00
G 80 FA 20	1.33
G 60 FA 40	4.50
G 40 FA 60	9.40
G 20 FA 80	11.5

321

322 **3.2 Short-term reactivity and strength development**

323 The reactions triggered by alkali activation are mainly exothermic. Monitoring the heat
324 release is thus a useful method to understand the transformations of alkali activated materials
325 at early ages. In this section, the data provided by isothermal calorimetry are thus presented
326 and compared with the strength development of the studied mixtures and their microstructure
327 observed with SEM. All the results are related to the stable grouts described in Table 3. It
328 should be noted that calorimetric responses were found to be independent from the xanthan
329 gum content [2]. This study actually showed that the used stabilizer did not act on the packing
330 density of the powders, by a deflocculating effect for example. The contact area between the

powders and the activator was not influenced by the stabilizer and thus the reaction rate was not affected.

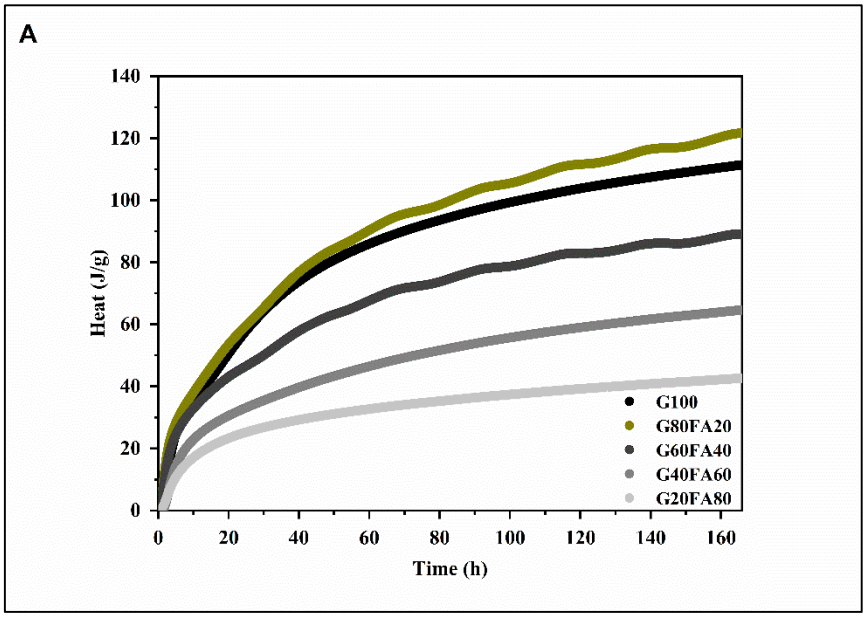

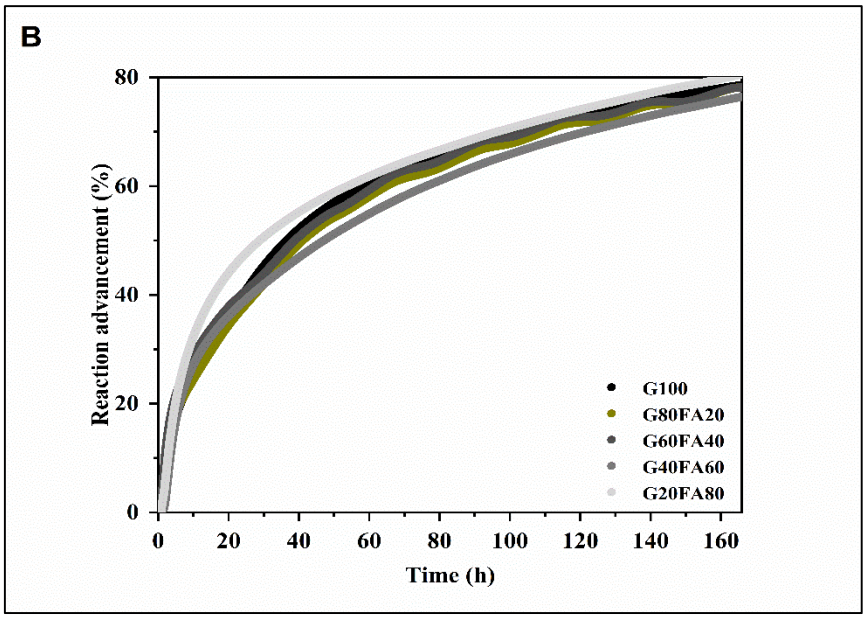

Figure 5. Released heat per unit weight of grout (A) and Reaction advancement (B)

The cumulated heat at 7 days has been directly deduced from cumulated heat experimental data (Figure 5.A) and the cumulated heat at 28 days has been determined by extrapolation using $1/\sqrt{t}$ function [37]. This extrapolation will allow to compare the heat release (Table 7)

and strength development at 7 and 28 days. The data highlight an optimum released heat of the G80FA20 mixture, at 7 and 28 days. The reaction advancement (Figure 5.B) has been determined from the calorimetry data as the ratio of cumulated heat to ultimate heat, and plotted in Figure 5.B. The replacement of BFS by FA affected the ultimate heat (Table 7) but it had a lower influence on the reaction kinetics during the first seven days.

The general trend was a decrease of released heat with FA proportion. This indicates a lower reactivity of FA at early age. FA is known to be much less reactive, with a slow transformation kinetic compared to GGBFS [21]. However, if this was the only parameter affecting the heat release of studied mixtures, the mixture with 20% FA (G80FA20) would not show the highest value. G80FA20 showed higher values than G100FA00, which suggests that other phenomena influence the overall reactivity of the binary mixtures.

Zhang et al. [38] and Aboulayt et al. [2] actually observed that the variations of heat flow and cumulated heat were not proportional to fly ash content. The effect of fly ash was less pronounced for relatively low fly ash proportions, for instance 20%. On the one hand, the activator content and its composition were kept constant in all mixtures. This is likely to accelerate the reaction of the most reactive powder, here GGBFS, due to higher activator to GGBFS ratio. One the other hand the reduction of the GGBFS content, which is easily soluble in comparison with fly ash, results in lower concentrations of the silicate and aluminate species necessary for the geopolymerization, which is likely to delay and make slower the overall reaction of fly ash whose dissolution is generally affected by OH concentration. The Fly ash could dissolve even more using high NaOH concentrated solution.

It is generally agreed that the hydration of alkali activated GGBFS is close to that of Portland cement-based systems, although reaction products are not necessarily the same. This transformation includes several mechanisms such as the dissolution of slags by a hydroxylic

attack, the nucleation and growth of initial formed phases whose contours undergoes several chemical interactions and reagent diffusion into the formed products [39].

In the literature, three simultaneous and rapid stages have been proposed. The activation of fly ash is primarily initiated, under highly basic environment, by dissolution of silicates and aluminates species; the interest of this stage is to enrich the medium with sufficient reactive precursors. The second stage is the polycondensation and formation of a so-called gel phases due to the restructuration and the rearrangement of precursors. The last step is the hardening of the gel phase [40]

Table 7. 7 days (Q_{7d}), 28 days (Q_{28d}), and ultimate values (Q_{∞}) of released heat.

	Released heat (10^{-2} kJ/g)		
	Q_{7d}	**Q_{28d}**	**Q_{∞}**
G100FA00	11.13	12.65	14.17
G80FA20	12.03	13.80	15.56
G60FA40	8.86	10.14	11.41
G40FA60	6.50	7.48	8.459
G20FA80	4.29	4.79	5.29

Zhang et al. [38] observed that the partial replacement of metakaolin by fly ash decreases the contact surface area of solid particles with alkaline solution and the reactivity of solid raw materials, resulting in a lower initial reaction rate and a longer reaction duration. They found an optimum replacement level of 10%. At this proportion the beneficial effect of the increase in the reaction extent was higher than the decrease of the average reactivity of raw materials. This low FA proportion also leads to an optimum in compressive strength at 7 and 28 days.
Figure 6 shows the evolution of the compressive strengths of the stabilized grouts. Replacing GGBFS by FA globally leads to a lower strength. Compressive strength at 7 days reduces from 10.58 MPa to 1.47 MPa from 100 wt.% to 20wt.% of GGBFS, while at 28 days it decreases

384 from 14.47 MPa to 2.63 MPa. The evolution of the compressive strength presents an optimum
385 at a replacement rate of 20 wt.% after 7 days and shifts towards 40 wt.% after 28 days.
386

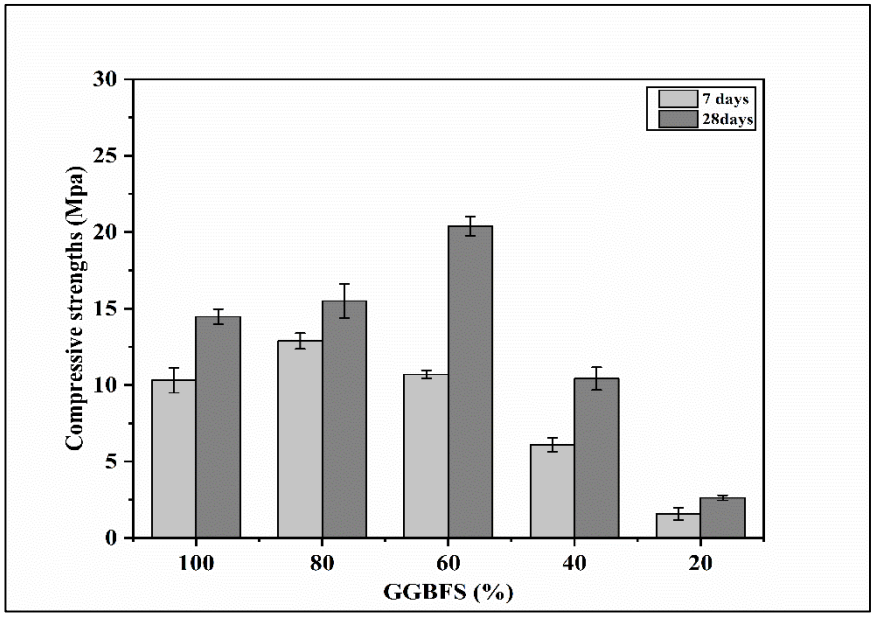

387

388 Figure 6. Compressive strengths at 7 and 28 days versus the GGBFS replacement.

389

390 Observed evolution can be explained by several reasons. One of the main factors is the
391 difference between the reactivity of GGBFS and FA. At 7 days the highest strength
392 corresponds to the optimum at cumulated heat release, whereas at 28 days the highest strength
393 corresponds to 40% of FA. Thus the evolution of mechanical properties cannot be only
394 correlated with the reactivity of the mixture; it could be due to different microstructures. Two
395 phenomena are likely to modify the evolution of the studied materials. With increasing fly ash
396 proportion, i) the activator to GGBFS ratio increases, which is likely to foster the reactivity of
397 slag at early age, while FA has not significantly reacted yet; ii) the packing density of the
398 powders mixture increases, as FA has higher packing density than GGBFS (see Table 2), the
399 unreacted FA particles are likely to reinforce the composite microstructure such as coarse

aggregates in concrete mixtures. Figure 7 shows the SEM pictures of polished samples at 28 days.

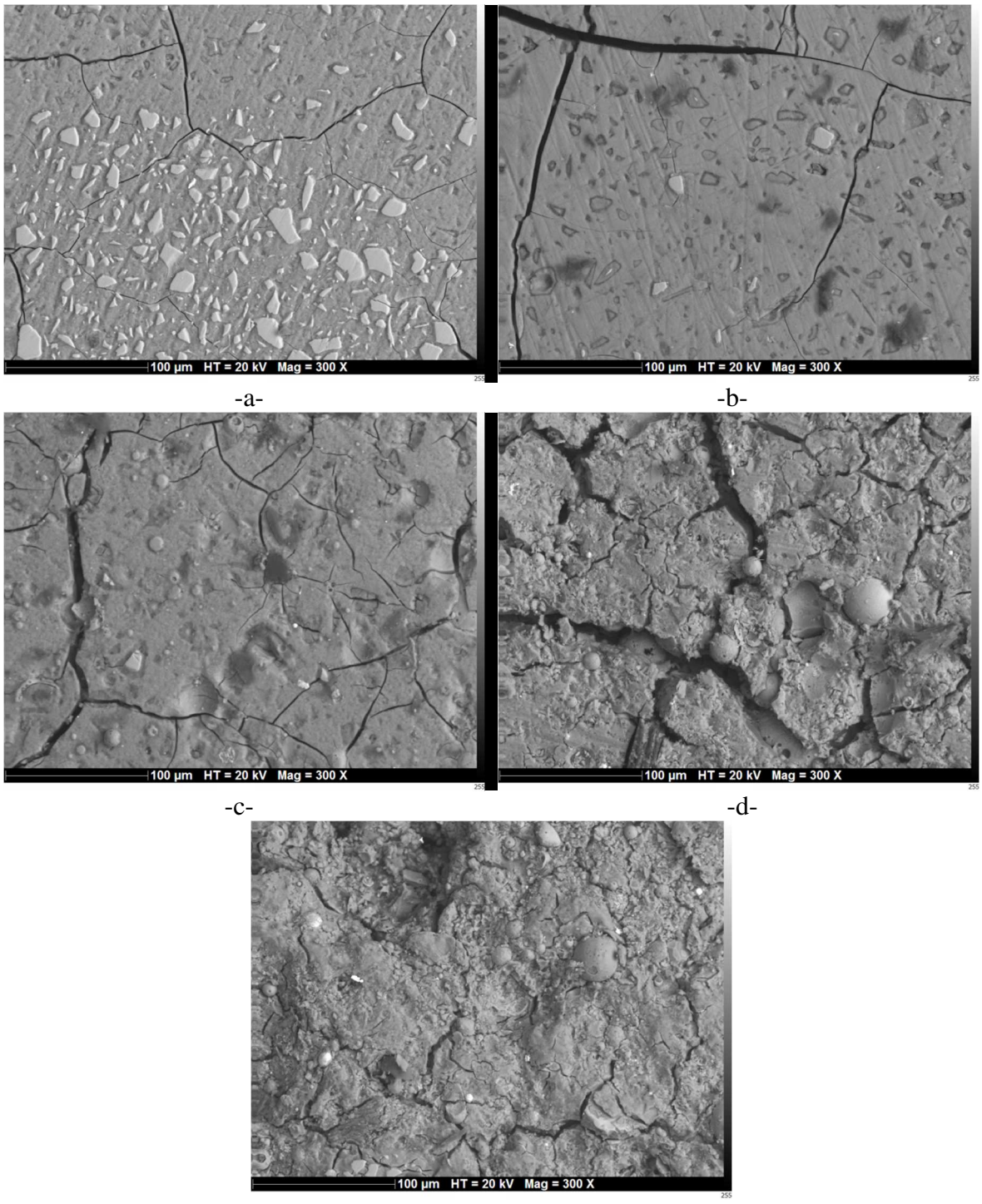

Figure 7. SEM pictures of studied grouts: (a) G100FA00 (b) G80FA20 (c) G60FA40 (d) G40FA60 (e) G20FA80.

411 Cracks can be observed in all specimens. They are due to drying shrinkage as grout samples
412 are exposed to low vacuum in SEM chamber. Unreacted GGBFS particles appear in light grey
413 and FA particles are mostly spherical. The proportion of unreacted GGBFS seems to decrease
414 from G100FA00 to G60FA40 due to the reactivity of the precursors as well as the dilution
415 effect imposed by the mix design limiting dissolution of FA. The SEM pictures of G80FA20
416 and G60FA40 mixtures show some coarse unreacted GGBFS and FA particles embedded in a
417 dense matrix. The most homogeneous aspect corresponds to G80FA20, which is consistent
418 with its highest strength. G40FA60 and G20FA80 show more porous matrix with numerous
419 partially reacted FA particles; these mixtures actually had significantly lower strengths.
420

421 **3.3 Products of alkali activation at long term (700 days)**

422 The microstructure of hardened grouts mainly consists in macroporosity, unreacted particles
423 and a more or less homogenous phase resulting from the reaction between activating solution
424 and precursors. This phase contains the products of alkali activation. Experimental techniques
425 such as NMR and XRD have been used to investigate its composition and understand the
426 reactivity of binary GGBFS-FA mixtures. The results presented in this section are related to
427 the stable grouts described in Table 3.
428

429 Figure 8 represents the XRD patterns of all the elaborated GGBFS-FA blends. Several
430 crystalline phases are overlapping with other phases in some diffraction angles.
431 As detected, the alkali activated slag grout contains an aluminum substituted tobermorite-like
432 phase ($Ca_5Si_5Al(OH)O_{17}\cdot 5H_2O$, PDF # 00-019-0052) as the main reaction product of the
433 alkali-activation of slag. G100FA00 XRD pattern shows the presence of characteristic peak of
434 calcite ($CaCO_3$, PDF# 00-005-0586), as the samples probably suffered a slight carbonation
435 [22].

When slag is replaced by fly ash, new crystalline phases are detected. The intensity of characteristic peaks of tobermorite decreases, especially between G60FA40 and G40FA60. Instead, new zeolitic crystalline structure similar to the garronite ($NaCa_{2.5}(Si_{10}Al_6)O_{32}\cdot 14H_2O$, PDF# 00-039-1374) appears for mixtures with high amount of fly ash (G40FA60 and G20FA80 mixtures), possibly resulting from the incorporation of sodium in C-A-S-H gel structure [41,42]. The formation of garronite, also known as zeolite P (NaP) [43], has been previously identified in sodium silicate activated slag/fly ash binders and cured at 30 °C [22]. Characteristic peaks of unreacted phases from FA particles are detected, namely quartz, mullite, and iron oxide (maghemite) are detected. The mineralogical characterization of mixtures with high fly ash content also highlights a noteworthy displacement of the fly ash amorphous hump from (15°-38°) to (21°-40°) 2θ ranges in FA-rich mixtures. This suggests that a new amorphous structure, different from that coming from fly ash, was formed. However it is difficult to detect C-S-H originating from the pozzolanic reaction and/or slag hydration by XRD analysis, because of their mainly amorphous character [44].

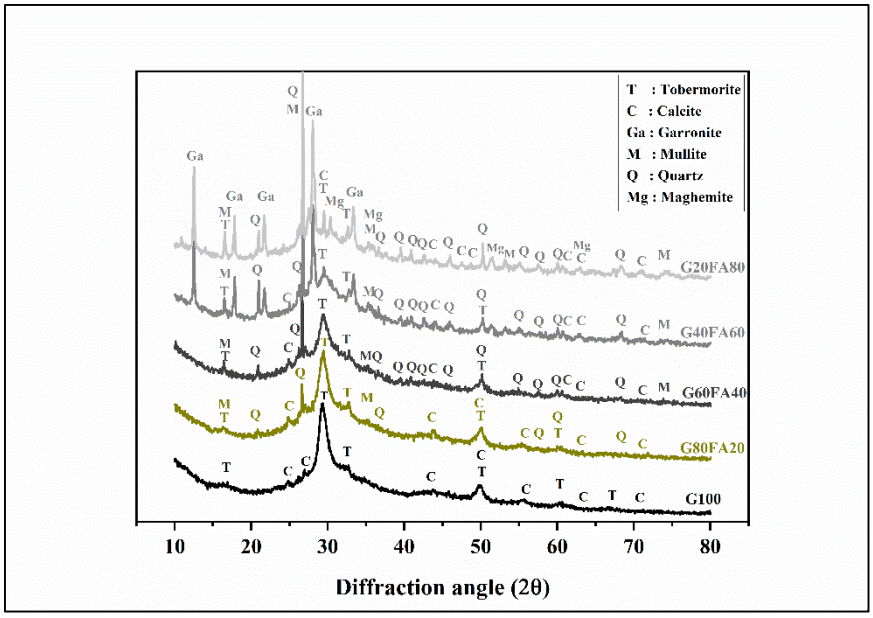

Figure 8. XRD patterns of elaborated grouts.

Figure 9 shows the FTIR analysis of the materials after 700 days. FTIR spectra of all mixtures show similar characteristics due to common alkali-activation products. They highlight a succession of several weak and strong bands between 450 and 4000 cm^{-1}.

The bands at approximatively 454 cm^{-1} are related to the deformation of SiO_4 tetrahedra. The band at 740 cm^{-1} identify the symmetric stretching vibrations of Si-O-Si and Al-O-Si [22,41]. The band at 1470 cm^{-1} is assigned to the asymmetric stretching mode of the O-C-O bonds of CO_3^{2-} groups. Carbonate is generally reflected in the infrared spectral region of (1410–1570) cm^{-1} [45,46]. The band between 900 cm^{-1} and 1300 cm^{-1} is assigned to the asymmetric stretching mode of the Si-O-T, where T is Si or Al, and reflects the formation of both C-(A)-S-H gels resulting from the activation of GGBFS and N-A-S-H gels as well as zeolites formed from the activation of fly ash [49–51]. This large band represents the main difference between the studied spectra. The band is centered at 960 cm^{-1} for materials containing 100 and 80% of GGBFS (G100FA00 and G80FA20 respectively) and it shifts slightly to higher frequencies (from 960 to 1000 cm^{-1}). The position at 960 cm^{-1} is typical of the asymmetrical stretching vibration of CASH gel. With the increase of the FA content that band is much more broader and shifts to higher wavenumber, probably as the result of the overlapping of several components; reaction products (CASH, NASH or (N;C)-A-S-H) and unreacted FA. The simultaneous activation of fly ash and slag leads to the formation of a geopolymer gel which contributes to decrease Al content incorporated into the C-A-S-H type gel, and induces its structural reorganization [22,41,42], The bands at 1650 cm^{-1} and the large one around 3450 cm^{-1} are characteristic of water vibration, in its bonded or adsorbed form [2]. The intensity of the band is high for G100FA00 and G80FA20 spectra, and low for G60FA40 to G20FA80 mixtures. Chemically bound water is mainly found is C-(A)-S-H structure, which is more clearly seen in samples with high GGBFS content as confirmed by XRD analyses (Figure 8).

All FTIR observed bands of this work and their attributions as well as references are summarized in Table 8.

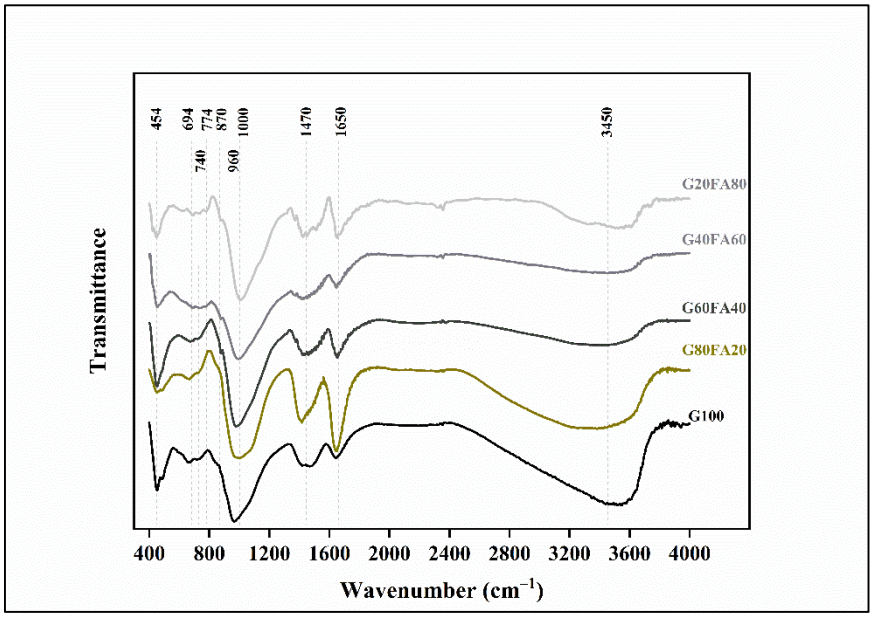

Figure 9. FTIR analysis of hardened grouts samples.

Table 8. Characteristic IR vibrational bands of stabilized formulations.

Wavenumber (cm^{-1})	Assignment	References
454	Bending vibration of Si-O-Si and O-Si-O	[41]
740	Symmetric stretching vibrations of Si-O-Si and Al-O-Si	[22,52]
870	Asymmetric stretching mode of the O-C-O bonds of carbonates	[45,46]
900-1300	Asymmetric stretching mode of the Si-O-T (T: tetrahedral Si or Al),	[49,50]
1470	Asymmetric stretching mode of the O-C-O bonds of carbonates	[45,46]
1650	-OH vibrations of water	[2,50]
3450		

^{27}Al and ^{29}Si MAS-NMR results of all GGBFS and FA blends are depicted in appendixes figures A.4 and A.5. The Figure 10 shows the ^{29}Si NMR spectrum of the G100FA00 grout , 6

new silicon environments are detected, in addition to a still unreacted slag. The peak of remaining unreacted slag is weak, as the transformation of slag has been promoted by the combined effect of the proportion and composition of the activation solution as well as the significant age of samples (700 days). The slag to activation solution ratio was relatively low.

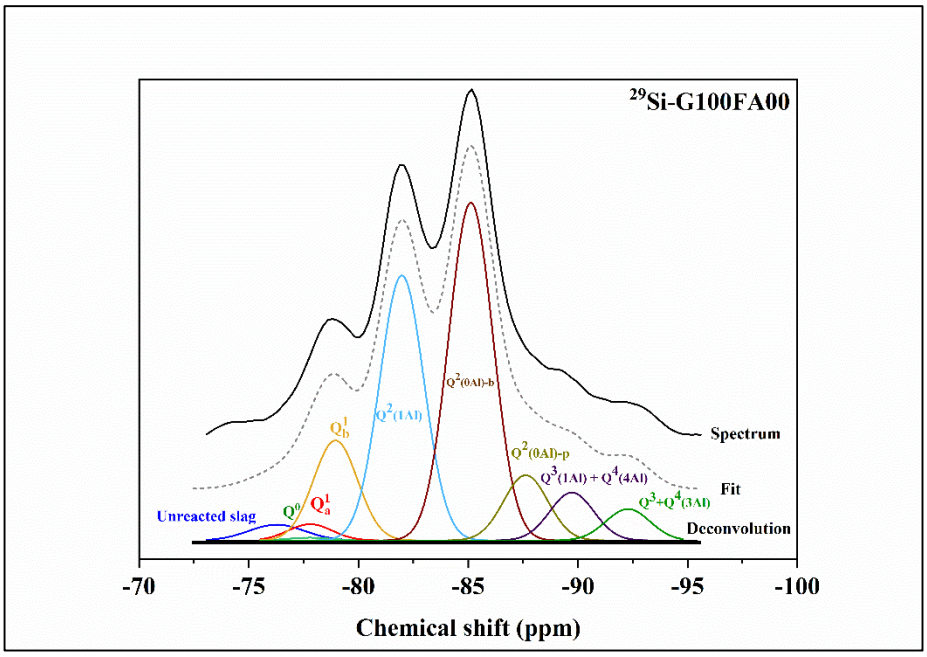

Figure 10. Deconvoluted ^{29}Si MAS NMR spectra of alkali activated G100FA00 blends

The deconvoluted peak located at -76.1 ppm is assigned to Q^0 sites; peaks at approximately -77.8 ppm and -79.0 ppm are attributed to silicate species in chain-end Q^1 of which two are often observed (Q^1_a and Q^1_b) [14,34]. Peaks located at a chemical shift of -82.0 ppm and -85.1 ppm are assigned to Q^2(1Al) and Q^2 respectively. It is reported that distinct resonances from Q^2 units can often be observed within C-A-S-H gels; they are assigned to the paired and bridging units [34,53]. The -89.7 ppm resonance is assigned to the crosslink Q^3(1Al) sites which are overlapping with a Q^4(4Al) sites. The presence of crosslink Q^3(1Al) sites in alkali activated slag was recently mentioned [54]. Q^4(4Al) units were included by considering the presence Q^4(3Al) sites at -92.3 ppm. Those four-connected silicates are related to the

505 formation of an additional polymerized Al-rich aluminosilicate phase. When fly ash is added,
506 peaks are clearly isolated, well-resolved and more pronounced at low chemical shifts when the
507 replacement of GGBFS by FA increases. For the GGBFS-FA blends, ^{29}Si deconvolution was
508 performed by considering a single peak for Q^1 and Q^2 peaks to achieve a good fitting as used
509 in several studies [14,23,35,55].
510 On the ^{27}Al spectrum of G100FA00 (Figure A.4), two distinct aluminum environments are
511 detected. An asymmetric band around +67 ppm is attributed to three tetrahedral aluminum
512 environments: unreacted slag underlying the spectra, Al(IV) incorporated in the Q^2(1Al) and
513 Q^3(1Al) units with bridging conditions inside (C,N)-A-S-H [56] gels as proven by ^{29}Si NMR
514 spectrum, and a third tetrahedral environment at +74 ppm (see below ^{29}Si MAS-NMR).
515 Walkey et al. [25] also observed a narrow resonance at +76 ppm attributed to the aluminum in
516 a well-defined tetrahedral coordination. The aluminate sharp, less intense peak and centered at
517 +10 ppm is assigned to aluminum with octahedral coordination within a secondary product of
518 the slag alkali-activation. This phase is not crystallized enough to be clearly detected by XRD.
519 It can be assigned to a hydrotalcite like phase due to the non-negligible MgO content of slag
520 (Table 2). Hydrotalcite is known to be a product of alkaline activation of Mg-rich slags, and
521 usually considered as a poorly crystallized phase and therefore difficult to detect by XRD [57].
522 The high sensitivity of ^{27}A1 NMR compared to ^{29}Si allows the detection of relatively small Al
523 contents in secondary reaction products [28].
524 When fly ash is added, we note a decrease of the intensity of Al(IV) species due to the quasi
525 disappearance of the peak at 74 ppm, indicating a probable decrease of C-A-S-H gels. It should
526 be noted that aluminum within amorphous N-A-S-H phases is known to appear below +60
527 ppm in ^{27}Al NMR MAS [23]. The peak at 10 ppm decreases and disappears for FA proportions
528 higher than 20%, probably due to the depleting of magnesium in the system related to the
529 replacement mod of GGBFS by Fly ash. In all samples, pentahedral aluminum is close to zero.

Table 9 summarizes the deconvolution results of alkali activated slag-fly ash blends. For G80FA20 and G60FA40, the predominant newly formed Q^0, Q^1, Q^2(Al), Q^2 and Q^3(1Al) groups identify the main reaction products of alkali-activated slag. These can be described as poorly crystalline calcium silicate hydrates with dreierketten-type structure and close to a tobermorite like structure [54,55,58]. The products resulting from the alkali activation of fly ash appear around -90 ppm, -94 ppm, -98 ppm and -102 ppm. They are assigned to silicate tetrahedra which are connected to tetrahedral aluminate (Q^4(nAl)) where n = 1, 2, 3, and 4), announcing therefore the structuration of geopolymer as well as a zeolites products known to be detectable between -85 ppm and -110 ppm [36]. The detection of Q^3(1Al) units in the structure of calcium silicate hydrates formed in alkali activated slag suggests the existence of tetrahedral Al in bridging positions as well as the possible formation of cross-linked structures, in particular when water glass is used as an activator [59]. The activation of slag can lead to the formation additional crosslinking sites of Q^4(4Al) and Q^4(3Al) [57,60].

Table 9. Si environments within the reaction products (%)

	G100FA00	**G80FA20**	**G60FA40**	**G40FA60**	**G20FA80**
Q^1	13.11	4.52	4.79	4.80	1.04
Q^2(1Al)	29.88	14.33	6.67	4.84	1.56
Q^2	45.45	44.54	39.28	19.76	4.92
Q^3(1Al)	3.63	13.32	12.75	0.11	0.40
Total C-A-S-H (%)	**92.07**	**76.71**	**63.49**	**29.51**	**7.92**
Si/Al_{CASH}	**5.92**	**8.85**	**15.22**	**12.14**	**9.64**
MCL	**15.77**	**31.22**	**22.59**	**13.27**	**15.98**
Q^4(4Al)	1.78	5.00	6.06	10.00	0.40
Q^4(3Al)	3.55	9.99	12.11	20.01	0.81
Q^4(2Al)	0.00	4.57	9.55	22.47	31.46
Q^4(1Al)	0.00	1.68	4.61	4.58	24.96
Q^4(0Al)	0.00	0.00	3.44	4.58	11.51
Total N-A-S-H* (%)	**5.33**	**21.24**	**35.77**	**61.64**	**69.14**
Si/Al_{NASH}	**1.20**	**1.40**	**1.70**	**1.65**	**3.01**

*Estimations assume that all the amorphous phases react, they do not take into account the contribution of unreacted precursors and consider the formation of pure N-A-S-H species.

From G80FA20 to G20FA80, Q^2(Al), Q^2 and Q^3(1Al) exhibit an obvious decrease while Q^4(1Al), Q^4(2Al) and Q^4(3Al) contributions clearly increase, especially between G40FA60 and G60FA40. The observed drop of slag reaction products could be expected as fly ash was used as a replacement of slag, the major source of calcium. The increase of the clear and isolated Q^4 peaks reflects a higher crosslinking and polymerization in the blended system. Q^4(0Al) species detected at chemical shifts higher than -108 ppm are assigned to different crystalline phases of silica [61].

Based on the deconvolution results of ^{29}Si MAS NMR spectra, it is possible to quantify the reaction products in alkali activated slag-fly ash blends to which some difficulties are often related. On the one hand, regarding the decomposition of ^{29}Si spectra, Si sites of remaining raw materials (FA) could overlap with their equivalent in the newly formed structures, in particular in chemical shifts between -90 ppm and -109 ppm. On the other hand, the second difficulty concerns the consideration of a model to describe the structure of alkali-activation products, for both slag and fly ash. Even if the literature on alkali-activated materials generally agree on the Engelhardt's description for N-A-S-H gels [28], it was also reported that calcium readily displaces sodium by ion exchange on the N–A–S–H gels leading to (N, C)–A–S–H gels that can coexist with C–A–S–H gels [62], especially in high Ca -content mediums, increasing Ca content in the precursor can in fact lead to impede formation of N-A-S-H [25]. In addition to that, the main reaction products of slags alkali activation (C-A-S-H) were subject of debate between several studies.

To overcome the quantification difficulties of the main reaction products, estimations do not take into account the contribution of unreacted precursors and assume that all the amorphous phases react. Calculations consider also that the geopolymerization of fly ash leads to a pure

N-A-S-H that entirely transform to (N, C)–A–S–H. Two models are considered, The substituted general model (SGM) and the Engelhardt's description. The substituted general model is widely used in cement chemistry and still considered even recently for the quantification of the alkali activated slag-fly ash composites [57].

Si/Al_{CASH} and mean chain length (MCL_{CASH}) are calculated using equations 2 and 3 respectively.

$$\frac{Si}{Al_{CASH}} = \frac{Q^1+Q^2(1Al)+Q^2}{\frac{1}{2}Q^2(1Al)} \quad (2)$$

$$MCL_{CASH} = \frac{Q^1+\frac{3}{2}Q^2(1Al)+Q^2}{\frac{1}{2}Q^1} \quad (3)$$

Si/Al $_{NASH}$ is calculated from Engelhardt's (equation 4) [28]. Q^3(1Al) quantities were deducted from Q^4(4Al) which in turn were calculated from Q^4(3Al) quantities using (equation 5). The correlation was proposed by [63] and used by several studies to this purpose, where $I_{Q^4(4Al)}$ is the intensity of the Q^4(3Al) determined from deconvolution of the ^{29}Si MAS NMR data with ($(Si/Al)^*$=1.2) and consistent with the composition of N-A-S-H gels in alkali-activated metakaolin [14,35].

$$\frac{Si}{Al_{NASH}} = \frac{\sum_{n=0}^{4} Q^4(nAl)}{\sum_{n=0}^{4} \frac{n}{4}Q^4(nAl)} \quad (4)$$

$$I_{Q^4(4Al)} = I_{Q^4(3Al)} \cdot \left[\frac{\frac{3}{5}(Si/Al)^* - 1}{1-(Si/Al)^*}\right] \quad (5)$$

Results of the quantification of reaction products are summarized in Table 9. It should also be noted that the limitation of the experimental results lies in the estimation of the remaining FA contribution. Faced with this issue, the amorphous fraction of raw materials was assumed to react completely and the contribution of remaining fly ash is therefore neglected, thus the

593 Q^4(0Al) associated to the crystallized compounds (shifts higher than -108 ppm) is not taken
594 into consideration in the calculation of Si/Al_{NASH} where it was also assumed that pure NASH
595 gels were obtained. This approximation seems to reproduce the considerable reactivity of fly
596 ash at long term, as new crystalline products appear in XRD patterns of G20FA80 and
597 G40FA60; they could result from the decomposition of fly ash. As the slag replacement
598 increases (Table 9), on the one hand, total C-A-S-H gel product decreases and N-A-S-H
599 increases. Si/Al_{CASH} varies from 5.92 for G100FA00 to 15.22 for G60FA40 while MCL
600 represents an optimum for G80FA20. On the other hand, Si/Al_{NASH} increases with fly ash
601 proportion from 1.20 for G100FA00 to 3.01 for G20FA80.

602 Several models have been proposed to describe the products of the alkali-activation of low and
603 high calcium alumino silicates. The substituted general model (SGM) proposed by Richardson
604 and Groves provides a description of the structural calcium–sodium aluminosilicate hydrate
605 gels [64]. In turn, based on NMR analysis, A. Fernandez-Jiménez et al [59] confirmed the
606 presence of Q^3(1Al) units in the structure of calcium silicate hydrates formed in alkali
607 activated slag. It was also found that the detection of Q^3 silicon units indicate the possible
608 formation of cross-linked structures, especially with waterglass used as an activator. An
609 alternative structural model has been recently proposed by Myers et al, the cross-linked
610 substituted tobermorite model (CSTM) which describes the C-(N)-A-S-H as a tobermorite like
611 structure consisting of cross linked and non-cross linked species. CSTM could be a relevant
612 tool as the experimental study of Myers et al. also concerned sodium silicate-activated slag
613 pastes. Their ^{29}Si and ^{27}Al NMR spectra had common features with the spectra plotted in
614 Figure 11. However the results cannot be directly compared for several reasons.
615 First their raw materials had different composition and the analysis was made at 56 days. Here
616 at 700 days the unreacted slag content of G100FA00 sample was very low. Previous study [16]
617 has also shown a significant evolution of nanostructure with curing time. The decrease of Q^3

618 fraction and the rise of the Q^2(1Al) fraction suggested a later stage of aluminum incorporation
619 in the C-A-S-H phase. The Q^2(1Al) fraction of G100FA00 sample was actually significant
620 (Table 9). Myers et al. suggested the presence of an additional aluminum-containing activation
621 product in alkali silicate activated slag binders to explain the difference between the average
622 composition of the binder and the calculated composition from the CSTM. It is likely that this
623 phase turned into C-A-S-H phase at long-term.
624

625 **3.4 Discussion**

626 The studied materials cover a wide range of compositions and properties as the fly ash
627 proportion varies from 0 to 100%. This results in significant variations of the engineering
628 properties as well as the phase composition of the products of alkali activation.
629 The stabilizer considered in this study allowed meeting the specifications for fresh and early-
630 age properties. For most of studied grouts, a 0.4 wt.% content of xanthan gum was enough to
631 achieve high slag replacement rates without causing bleeding. As a consequence, G80FA20
632 and G60FA40 can be considered as the best mixtures among the studied grouts for several
633 reasons. Their performances are actually in good agreement with the operating specifications
634 established at the beginning of this study. G60FA40 actually showed the highest mechanical
635 strength, even if the Marsh flow time was higher due to the amount of 0.4 wt.% of xanthan
636 gum. Adding a thickening agent to minimize the bleeding can be associated, if required, with
637 the use of a deflocculating admixture or superplasticizer to improve the flow properties. In
638 addition to that, regarding the physicochemical characterization (XRD, FTIR, and NMR),
639 G60FA40 combines a variety of binding phases which will undoubtedly allow to exploit, on
640 the one hand, the benefits of rapid hardening of GGBFS and the strengthening character of
641 their alkali-activation products, and in the other hand, the excellent reputation of reaction
642 products from activated fly ash especially their physico-chemical stability [65].

643 The characterization of their nanostructure at long-term (700 days) allows dividing the studied
644 materials into three groups: i) G100FA00, ii) G80FA20 and G60FA40, iii) G40FA60 and
645 G20FA80. The results showed in section 3.3 can also be compared with other studies on slag-
646 fly ash composites [22] and synthetic calcium and sodium aluminosilicates [24,25]. Note that
647 Ismail et al. [22] did not use NMR thus they could not identify and quantify the relative
648 proportions of C-A-S-H and N-A-S-H phases.
649 The values of Ca/Si, Ca/(Si+Al), Al/Si, and Na/Al (Table 4) were used to compare the results
650 from this study with literature. The actual ratios are likely to vary during curing time, as
651 GGBFS and FA mainly react at short-term and long-term respectively. Here taking into
652 account FA (or not) does not strongly affect the molar composition of the mixture (Table 4).
653 The G100FA00 samples correspond to a high-calcium system. The products mainly consist in
654 aluminum substituted tobermorite-like phase, as confirmed by XRD and NMR analyses. The
655 ^{29}Si NMR spectrum showed well-defined peaks corresponding mainly to Q^1 and Q^2. The
656 quantitative analysis (Table 9) suggests that this tobermorite-like phase (C-A-S-H) represents
657 nearly 94% of gel phase. This nanostructure seems consistent with the $CaO\text{-}SiO_2\text{-}Al_2O_3$
658 diagrams provided by Garcia-Lodeiro et al. [24] even if they used synthetic materials instead
659 of industrial products used here.
660 G80FA20 and G60FA40 show that a relatively low FA proportion can significantly affect the
661 properties and phase composition of GGBFS-based materials. This does not appear in XRD
662 spectra, although the intensity of the main tobermorite peak decreased, but the NMR spectra
663 clearly indicate a significant change in gel structure. The well-structured crystalline C-(N)-A-
664 S-H and the well-resolved Q^1 and Q^2 peaks cannot be observed anymore in ^{27}Al NMR and ^{29}Si
665 NMR spectra respectively. This is mainly due to the drop in Q^2(1Al) proportion from
666 G100FA00 to G80FA20 samples. Walkley et al. [25] actually showed that high Ca content
667 favors the incorporation of aluminum within the C-(N)-A-S-H gel. The quantitative analysis

668 (Table 9) also shows a drop in C-A-S-H phase and a significant increase in N-A-S-H
669 proportion, thus the aluminum, which could not be inserted in the C-A-S-H phase due to lower
670 calcium content, allowed the formation of N-A-S-H. This is consistent with the diagrams of
671 Garcia-Lodeiro et al. [24] as they predict a mixture of N-A-S-H and C-A-S-H with the initial
672 molar compositions of G80FA20 and G60FA40. These samples are closer to the C-A-S-H
673 region; the quantitative analysis (Table 9) actually showed that C-A-S-H proportion is higher
674 than N-A-S-H. Thus, the similarities between the products from synthetic materials and
675 industrial ones can be considered as a finding of the study. The results actually tend to show
676 that the position in the $CaO - SiO_2 - Al_2O_3$ diagram (Table 4) could be used to give a
677 reasonable view of the phase assemblages, even with industrial products instead of pure
678 synthetic phases.
679 G40FA60 and G20FA80 show different phases as GGBFS content is even reduced. This
680 clearly appeared in XRD and NMR spectra. A crystalline zeolitic structure identified as
681 Garronite appeared as a possible product of the incorporation of sodium in C-A-S-H structure.
682 The intensity of tobermorite peak (see XRD analyses on Figure 8) and the C-A-S-H content
683 (Table 9) actually dropped. The ^{29}Si NMR results showed new well-resolved peaks
684 corresponding to tetrahedral silicate connected to tetrahedral aluminates $Q^4(nAl)$. Higher
685 $Q^4(nAl)$ contents have already been associated with lower Ca/(Al+Si) ratios for synthetic
686 precursors [25]. However, G40FA60 shares with G60FA40 sample significant Q^2 and C-A-S-
687 H contents, which nearly disappear in G20FA80. This could partly explain the drop in
688 strength (Figure 6). The composition of G60FA40 lies between C-A-S-H and N-A-S-H
689 regions [24] whereas G80FA20 reaches the limit of N-A-S-H region. The quantitative
690 analysis (Table 9) actually showed that C-A-S-H proportion is lower than N-A-S-H,
691 especially for G80FA20. The use of NMR actually allowed investigating C-N-A-S-H phases
692 which could not be clearly distinguished in existing literature on binary mixtures. The

693 replacement of GGBFS by FA resulted in lower Ca/(Si+Al) ratios. This region of the CaO-
694 SiO_2-Al_2O_3 diagram actually favors the formation of three-dimensionally structured gel N-A-
695 S-H. Significant Q^3(1Al) contents could be found in the slag-fly ash samples, especially
696 G80FA20 and G60FA40, but this peak overlaps with Q^4(4Al). The intensity of Q^4(nAl)
697 actually increased with FA proportion. Myers et al. suggested that the additional Al-rich phase
698 could be a zeolite-like product with Si/Al ratio close to 1, also observed in gels formed
699 through alkali-activation of low-calcium aluminosilicate precursors. The Si/Al ratios of N-A-
700 S-H phase deduced from deconvolution (Table 9) were actually between 1 and 2 (excepted
701 G20FA80). This confirms that the slag-fly ash binary mixtures lead to a mixed nanostructure
702 (N,C)-A-S-H, reflected by (N-A-S-H), co-existing with C-A-S-H gels at long-term which is in
703 good agreement with previous studies [27,56,62].

704

705 **4. Conclusion**

706 Stable grouts with high water-to-solid ratios were designed and characterized to investigate the
707 influence of fly ash proportion on engineering properties, microstructure and phase
708 composition of sodium-silicate activated ground-granulated blast furnace slag. From the results
709 of the experimental study and their analysis the following conclusions can be drawn.

710 • As the grouts are meant to be used for soil improvement, the main specifications were
711 the stability and the fluidity at fresh state and the short-term compressive strength. The
712 use of xanthan gum-based admixture allowed designing stable grouts for all fly ash
713 proportions from 0 to 100%.
714 • The short-term strength was mainly provided by the reactivity of slag, as confirmed by
715 isothermal calorimetry. However the strength could not be directly correlated with heat

716 release, which suggests that fly ash particles had a beneficial influence on the
717 microstructure.

718 • The maximum strength was reached with 20 to 40% of fly ash. The change of materials
719 properties above 40% of fly ash was confirmed by the study of phase composition of
720 alkali-activation products. The replacement of slag by 20 to 40% of fly ash lead to
721 prevailing C-A-S-H phase combined with N-A-S-H. Above 40% of fly ash the
722 proportion of C-A-S-H dropped, N-A-S-H increased as well as the proportion of
723 unreacted material.

724 • The phase composition was compared with existing diagrams obtained on synthetic
725 phases. Although high water-to-solid ratios and the use of industrial byproducts instead
726 of pure phases, the long-term compositions of the materials of the present study are
727 consistent with some diagrams provided by previous works. These diagrams actually
728 predicted a mixture of C-A-S-H and N-A-S-H phases, which was actually deduced in
729 this study from the analysis of NMR results. It should be noted that the studied
730 mixtures could have not reached yet their equilibrium.

731 **Acknowledgements**

732 Erasmus mundus (Eu-METALIC II) program is acknowledged for the financial support of Dr.
733 Abdelilah Aboulayt's post-doctoral mobility. This study has also been partially funded by
734 Soletanche Bachy company.

735 **Declarations of interest:** none

736 **References:**

737

738 [1] A. Cherki El Idrissi, E. Roziere, A. Loukili, S. Darson, Design of geopolymer grouts :
739 the effects of water content and mineral precursor, 8189 (2016).
740 doi:10.1080/19648189.2016.1214183.

741 [2] A. Aboulayt, R. Jaafri, H. Samouh, A. Cherki, E. Idrissi, E. Roziere, R. Moussa, A.
742 Loukili, Stability of a new geopolymer grout : Rheological and mechanical
743 performances of metakaolin-fly ash binary mixtures, Constr. Build. Mater. 181 (2018)
744 420–436. doi:10.1016/j.conbuildmat.2018.06.025.

745 [3] K.H. Khayat, Viscosity-Enhancing Admixtures for Cement-Based Materials - An
746 Overview, Cem. Concr. Compos. 20 (1998) 171–188.

747 [4] J. Simon, B. Cerles, Gomme xanthane, Tech. l'ingenieur. J6670 V1 (2000) 1–10.

748 [5] P.F.G. Banfill, Rheology of Fresh Cement and Concrete, Rheol. Rev. 2006 (2006) 61–
749 130. doi:10.4324/9780203473290.

750 [6] K.H. Khayat, A. Yahia, Effect of Welan Gum-High-Range Water Reducer
751 Combinations on Rheology of Cement Grout, ACI Mater. J. (1997) 365–372.

752 [7] C.F. Ferraris, K.H. Obla, R. Hill, The influence of mineral admixtures on the rheology
753 of cement paste and concretef, Cem. Concr. Res. 31 (2001) 245–255.
754 doi:10.1016/S0008-8846(00)00454-3.

755 [8] P. Ghadir, N. Ranjbar, Clayey soil stabilization using geopolymer and Portland cement,
756 Constr. Build. Mater. 188 (2018) 361–371. doi:10.1016/j.conbuildmat.2018.07.207.

757 [9] M. Yaghoubi, A. Arulrajah, M.M. Disfani, S. Horpibulsuk, S. Darmawan, J. Wang,
758 Impact of field conditions on the strength development of a geopolymer stabilized
759 marine clay, Appl. Clay Sci. 167 (2019) 33–42. doi:10.1016/j.clay.2018.10.005.

760 [10] D.D.Æ.I.G.Æ.D. Panias, Polymerization in sodium silicate solutions : a fundamental
761 process in geopolymerization technology, (2009) 3719–3730. doi:10.1007/s10853-009-
762 3497-5.

763 [11] F. Rifai, A. Darquennes, B. Muzeau, L. Stefan, F. Benboudjema, Early-age cracking
764 tendency of alkali-activated slag binders compared to ordinary portland cement, in:
765 SynerCreteí18 Int. Conf. Interdiscip. Approaches Cem. Mater. Struct. Concr., Funchal,

766 Madeira Island, Portugal, 2018: pp. 413–418.

767 [12] S. Wang, K.L. Scrivener, Al NMR study of alkali-activated slag, 33 (2003) 769–774.
768 doi:10.1016/S0008-8846(02)01044-X.

769 [13] R. Taylor, I.G. Richardson, R.M.D. Brydson, Cement and Concrete Research
770 Composition and microstructure of 20-year-old ordinary Portland cement – ground
771 granulated blast-furnace slag blends containing 0 to 100 % slag, Cem. Concr. Res. 40
772 (2010) 971–983. doi:10.1016/j.cemconres.2010.02.012.

773 [14] R.J. Myers, S.A. Bernal, R. San Nicolas, J.L. Provis, Generelized structural description
774 of C-(N)-A-S-H gels: The crosslinked substituted tobermorite model, Langmuir. 29
775 (2013) 5494.

776 [15] N. Cristelo, S. Glendinning, A. Teixeira Pinto, Deep soft soil improvement by alkaline
777 activation, (2011). doi:10.1680/grim.900032.

778 [16] A. Cherki El Idrissi, M. Paris, E. Rozière, D. Deneele, S. Darson, A. Loukili, Alkali-
779 activated grouts with incorporated fl y ash : From NMR analysis to mechanical
780 properties, Mater. Today Commun. 14 (2018) 225–232.
781 doi:10.1016/j.mtcomm.2018.01.012.

782 [17] J.L. Provis, S.A. Bernal, Geopolymers and Related Alkali-Activated Materials, Annu.
783 Rev. Mater. Res. 44 (2014) 299–327. doi:10.1146/annurev-matsci-070813-113515.

784 [18] S. Samantasinghar, S.P. Singh, Fresh and Hardened Properties of Fly Ash–Slag
785 Blended Geopolymer Paste and Mortar, Int. J. Concr. Struct. Mater. 13 (2019) 1–12.
786 doi:10.1186/s40069-019-0360-1.

787 [19] R.R. Lloyd, J.L. Provis, J.S.J. Van Deventer, Acid resistance of inorganic polymer
788 binders. 1. Corrosion rate, Mater. Struct. Constr. 45 (2012) 1–14. doi:10.1617/s11527-
789 011-9744-7.

790 [20] J.I. Escalante García, K. Campos-Venegas, A. Gorokhovsky, A. Fernández,
791 Cementitious composites of pulverised fuel ash and blast furnace slag activated by
792 sodium silicate: effect of Na 2 O concentration and modulus , Adv. Appl. Ceram. 105
793 (2006) 201–208. doi:10.1179/174367606x120151.

794 [21] S. Kumar, R. Kumar, S.P. Mehrotra, Influence of granulated blast furnace slag on the
795 reaction, structure and properties of fly ash based geopolymer, J. Mater. Sci. 45 (2010)

796 607–615. doi:10.1007/s10853-009-3934-5.

797 [22] I. Ismail, S.A. Bernal, J.L. Provis, R. San Nicolas, S. Hamdan, J.S.J. Van Deventer,
798 Modification of phase evolution in alkali-activated blast furnace slag by the
799 incorporation of fly ash, Cem. Concr. Compos. 45 (2014) 125–135.
800 doi:10.1016/j.cemconcomp.2013.09.006.

801 [23] S.A. Bernal, J.L. Provis, B. Walkley, R. San Nicolas, J.D. Gehman, D.G. Brice, A.R.
802 Kilcullen, P. Duxson, J.S.J. Van Deventer, Gel nanostructure in alkali-activated binders
803 based on slag and fly ash, and effects of accelerated carbonation, Cem. Concr. Res. 53
804 (2013) 127–144. doi:10.1016/j.cemconres.2013.06.007.

805 [24] I. Garcia-Lodeiro, A. Palomo, A. Fernández-Jiménez, D.E. MacPhee, Compatibility
806 studies between N-A-S-H and C-A-S-H gels. Study in the ternary diagram Na2O-CaO-
807 Al2O3-SiO 2-H2O, Cem. Concr. Res. 41 (2011) 923–931.
808 doi:10.1016/j.cemconres.2011.05.006.

809 [25] B. Walkley, R. San Nicolas, M.A. Sani, G.J. Rees, J. V. Hanna, J.S.J. van Deventer,
810 J.L. Provis, Phase evolution of C-(N)-A-S-H/N-A-S-H gel blends investigated via
811 alkali-activation of synthetic calcium aluminosilicate precursors, Cem. Concr. Res. 89
812 (2016) 120–135. doi:10.1016/j.cemconres.2016.08.010.

813 [26] I. García-Lodeiro, A. Fernández-Jiménez, A. Palomo, Cement and Concrete Research
814 Variation in hybrid cements over time . Alkaline activation of fl y ash – portland
815 cement blends, Cem. Concr. Res. 52 (2013) 112–122.
816 doi:10.1016/j.cemconres.2013.03.022.

817 [27] I. Garcia-Lodeiro, D. Shane, A. Fernández-Jiménez, Á.. Palomo, Hydration of Hybrid
818 Alkaline Cement Containing a Very Large Proportion of Fly Ash : A Descriptive
819 Model, (2016). doi:10.3390/ma9070605.

820 [28] G. Engelhardt, Multinuclear solid-state NMR in silicate and zeolite chemistry, Trends
821 Anal. Chem. 8 (1989) 343–347. doi:10.1016/0165-9936(89)87043-8.

822 [29] A. Gharzouni, L. Ouamara, I. Sobrados, S. Rossignol, Alkali-activated materials from
823 different aluminosilicate sources: Effect of aluminum and calcium availability, J. Non.
824 Cryst. Solids. 484 (2018) 14–25. doi:10.1016/j.jnoncrysol.2018.01.014.

825 [30] A. Koenig, A. Herrmann, S. Overmann, F. Dehn, Resistance of alkali-activated binders

826 to organic acid attack: Assessment of evaluation criteria and damage mechanisms,
827 Constr. Build. Mater. 151 (2017) 405–413. doi:10.1016/j.conbuildmat.2017.06.117.

828 [31] M. Vafaei, A. Allahverdi, P. Dong, N. Bassim, Acid attack on geopolymer cement
829 mortar based on waste-glass powder and calcium aluminate cement at mild
830 concentration, Constr. Build. Mater. 193 (2018) 363–372.
831 doi:10.1016/j.conbuildmat.2018.10.203.

832 [32] N. Roussel, R. Le Roy, The Marsh cone: a test or a rheological apparatus?, Cem.
833 Concr. Res. 35 (2005) 823–830. doi:10.1016/j.cemconres.2004.08.019.

834 [33] F. Puertas, M. Torres-Carrasco, Use of glass waste as an activator in the preparation of
835 alkali-activated slag. Mechanical strength and paste characterisation, Cem. Concr. Res.
836 57 (2014) 95–104. doi:10.1016/j.cemconres.2013.12.005.

837 [34] X. Gao, Q.L. Yu, A. Lazaro, H.J.H. Brouwers, Investigation on a green olivine nano-
838 silica source based activator in alkali activated slag-fly ash blends: Reaction kinetics,
839 gel structure and carbon footprint, Cem. Concr. Res. 100 (2017) 129–139.
840 doi:10.1016/j.cemconres.2017.06.007.

841 [35] B. Walkley, A. Kashani, M.A. Sani, T.D. Ngo, P. Mendis, Examination of alkali-
842 activated material nanostructure during thermal treatment, J. Mater. Sci. 53 (2018)
843 9486–9503. doi:10.1007/s10853-018-2270-z.

844 [36] A. Buchwald, H. Hilbig, C. Kaps, Alkali-activated metakaolin-slag blends -
845 Performance and structure in dependence of their composition, J. Mater. Sci. 42 (2007)
846 3024–3032. doi:10.1007/s10853-006-0525-6.

847 [37] T. Lenormand, E. Rozière, A. Loukili, S. Staquet, Incorporation of treated municipal
848 solid waste incineration electrostatic precipitator fly ash as partial replacement of
849 Portland cement: Effect on early age behaviour and mechanical properties, Constr.
850 Build. Mater. 96 (2015) 256–269. doi:10.1016/j.conbuildmat.2015.07.171.

851 [38] Z. Zhang, H. Wang, Y. Zhu, A. Reid, J.L. Provis, F. Bullen, Using fly ash to partially
852 substitute metakaolin in geopolymer synthesis, Appl. Clay Sci. 88–89 (2014) 194–201.
853 doi:10.1016/j.clay.2013.12.025.

854 [39] A. Fernandez-Jimenez, F. Puertas, A. Arteaga, Determination of Kinetic Equations of
855 Alkaline Activation of Blast Furnace Slag by Means of Calorimetric Data, J. Therm.

856 Anal. Calorim. 52 (1998) 945–955. doi:10.1023/A:1010172204297.

857 [40] J.S.J. van D. John L. Provis, Geopolymers Structure, processing, properties and
858 industrial applications, woodhead Publishing, Oxford, 2009.

859 [41] S.K. Nath, S. Kumar, Influence of Granulated Silico-Manganese Slag on Compressive
860 Strength and Microstructure of Ambient Cured Alkali-Activated Fly Ash Binder,
861 Waste and Biomass Valorization. 0 (2018) 1–11. doi:10.1007/s12649-018-0213-1.

862 [42] S.K. Nath, S. Kumar, Reaction kinetics, microstructure and strength behavior of alkali
863 activated silico-manganese (SiMn) slag – Fly ash blends, Constr. Build. Mater. 147
864 (2017) 371–379. doi:10.1016/j.conbuildmat.2017.04.174.

865 [43] N.Y. Chen, T.F. Degnan, C.M. Smith, Molecular transport and reaction in zeolites :
866 design and application of shape selective catalysts, Wiley-VCH, 1994.
867 https://www.wiley.com/en-
868 fr/Molecular+Transport+and+Reaction+in+Zeolites%3A+Design+and+Application+of
869 +Shape+Selective+Catalysis-p-9780471185482 (accessed March 4, 2019).

870 [44] E. Coudert, M. Paris, D. Deneele, G. Russo, A. Tarantino, Use of alkali activated high-
871 calcium fly ash binder for kaolin clay soil stabilisation: Physicochemical evolution,
872 Constr. Build. Mater. 201 (2019) 539–552. doi:10.1016/j.conbuildmat.2018.12.188.

873 [45] V.F.F. Barbosa, K.J.D. MacKenzie, C. Thaumaturgo, Synthesis and characterisation of
874 materials based on inorganic polymers of alumina and silica: Sodium polysialate
875 polymers, Int. J. Inorg. Mater. 2 (2000) 309–317. doi:10.1016/S1466-6049(00)00041-
876 6.

877 [46] A. Aboulayt, M. Riahi, M. Ouazzani Touhami, H. Hannache, M. Gomina, R. Moussa,
878 Properties of metakaolin based geopolymer incorporating calcium carbonate, Adv.
879 Powder Technol. 28 (2017) 2393–2401. doi:10.1016/j.apt.2017.06.022.

880 [47] F. Puertas, M. Palacios, T. Vázquez, Carbonation process of alkali-activated slag
881 mortars, J. Mater. Sci. 41 (2006) 3071–3082. doi:10.1007/s10853-005-1821-2.

882 [48] S. Alonso, A. Palomo, Calorimetric study of alkaline activation of calcium hydroxide-
883 metakaolin solid mixtures, Cem. Concr. Res. 31 (2001) 25–30. doi:10.1016/S0008-
884 8846(00)00435-X.

885 [49] I. Ismail, S.A. Bernal, J.L. Provis, S. Hamdan, J.S.J. Van Deventer, Microstructural

886 changes in alkali activated fly ash/slag geopolymers with sulfate exposure, Mater.
887 Struct. Constr. 46 (2013) 361–373. doi:10.1617/s11527-012-9906-2.

888 [50] F. Puertas, A. Fernández-Jiménez, Mineralogical and microstructural characterisation
889 of alkali-activated fly ash/slag pastes, Cem. Concr. Compos. 25 (2003) 287–292.
890 doi:10.1016/S0958-9465(02)00059-8.

891 [51] A. Fernández-Jiménez, A. Palomo, Mid-infrared spectroscopic studies of alkali-
892 activated fly ash structure, Microporous Mesoporous Mater. 86 (2005) 207–214.
893 doi:10.1016/J.MICROMESO.2005.05.057.

894 [52] M. Criado, A. Fernández-Jiménez, A. Palomo, Alkali activation of fly ash: Effect of the
895 SiO2/Na2O ratio. Part I: FTIR study, Microporous Mesoporous Mater. 106 (2007)
896 180–191. doi:10.1016/j.micromeso.2007.02.055.

897 [53] J. Skibsted, M.D. Andersen, The Effect of Alkali Ions on the Incorporation of
898 Aluminum in the Calcium Silicate Hydrate (C-S-H) Phase Resulting from Portland
899 Cement Hydration Studied by ^{29} Si MAS NMR, J. Am. Ceram. Soc. 96 (2012) n/a-n/a.
900 doi:10.1111/jace.12024.

901 [54] G. Geng, R.J. Myers, J. Li, R. Maboudian, C. Carraro, D.A. Shapiro, P.J.M. Monteiro,
902 Aluminum-induced dreierketten chain cross-links increase the mechanical properties of
903 nanocrystalline calcium aluminosilicate hydrate, Sci. Rep. 7 (2017) 1–10.
904 doi:10.1038/srep44032.

905 [55] X. Pardal, F. Brunet, T. Charpentier, I. Pochard, A. Nonat, ^{27} Al and ^{29} Si Solid-State
906 NMR Characterization of Calcium-Aluminosilicate-Hydrate, Inorg. Chem. 51 (2012)
907 1827–1836. doi:10.1021/ic202124x.

908 [56] F. Puertas, M. Palacios, H. Manzano, J.S. Dolado, A. Rico, J. Rodríguez, A model for
909 the C-A-S-H gel formed in alkali-activated slag cements, J. Eur. Ceram. Soc. 31 (2011)
910 2043–2056. doi:10.1016/j.jeurceramsoc.2011.04.036.

911 [57] X. Gao, Q.L. Yu, H.J.H. Brouwers, Apply29Si,27Al MAS NMR and selective
912 dissolution in identifying the reaction degree of alkali activated slag-fly ash
913 composites, Ceram. Int. 43 (2017) 12408–12419. doi:10.1016/j.ceramint.2017.06.108.

914 [58] I.G. Richardson, G.W. Groves, The structure of the calcium silicate hydrate phases
915 present in hardened pastes of white Portland cement/blast-furnace slag blends, J. Mater.

916 Sci. 32 (1997) 4793–4802. doi:10.1023/A:1018639232570.

917 [59] A. Fernàndez-Jiménez, F. Puertas, Structure of Calcium Silicate Hydrates Formed in
918 Alkaline-Activated Slag: Influence of the Type of Alkaline Activator, J. Am. Ceram.
919 Soc. 94 (2003) 1389–1394. doi:10.1111/j.1151-2916.2003.tb03481.x.

920 [60] X. Ke, S.A. Bernal, J.L. Provis, Controlling the reaction kinetics of sodium carbonate-
921 activated slag cements using calcined layered double hydroxides, Cem. Concr. Res. 81
922 (2016) 24–37. doi:10.1016/J.CEMCONRES.2015.11.012.

923 [61] M. Criado, A. Fernández-Jiménez, A. Palomo, I. Sobrados, J. Sanz, Effect of the
924 SiO2/Na2O ratio on the alkali activation of fly ash. Part II: 29Si MAS-NMR Survey,
925 Microporous Mesoporous Mater. 109 (2008) 525–534.
926 doi:10.1016/j.micromeso.2007.05.062.

927 [62] I. García-Lodeiro, A. Fernández-Jiménez, A. Palomo, D.E. MacPhee, Effect of calcium
928 additions on N-A-S-H cementitious gels, J. Am. Ceram. Soc. 93 (2010) 1934–1940.
929 doi:10.1111/j.1551-2916.2010.03668.x.

930 [63] P. Duxson, J.L. Provis, G.C. Lukey, F. Separovic, J.S.J. Van Deventer, 29Si NMR
931 study of structural ordering in aluminosilicate geopolymer gels, Langmuir. 21 (2005)
932 3028–3036. doi:10.1021/la047336x.

933 [64] I.G. Richardson, A.R. Brough, G.W. Groves, C.M. Dobson, The characterization of
934 hardened alkali-activated blast-furnace slag pastes and the nature of the calcium silicate
935 hydrate (C-S-H) phase, Cem. Concr. Res. 24 (1994) 813–829. doi:10.1016/0008-
936 8846(94)90002-7.

937 [65] Fernandez-jimenez, I. Garcia-Lodeiro, A. Palomo, Durability of alkali-activated fly ash
938 cementitious materials, (2007) 3055–3065. doi:10.1007/s10853-006-0584-8.

939

Appendix A. Supplementary data

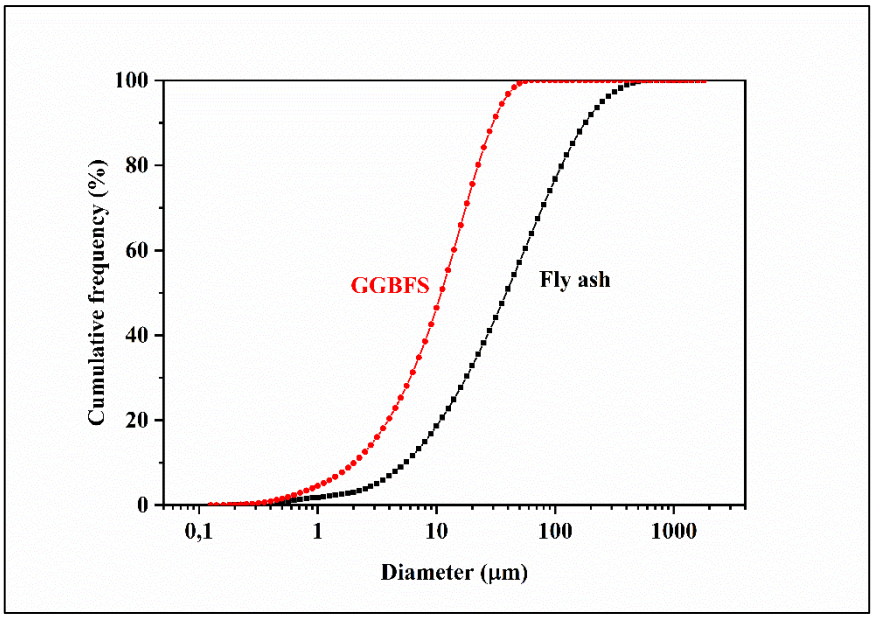

Figure A.1. Particle size distribution of granulated blast furnace and fly ash.

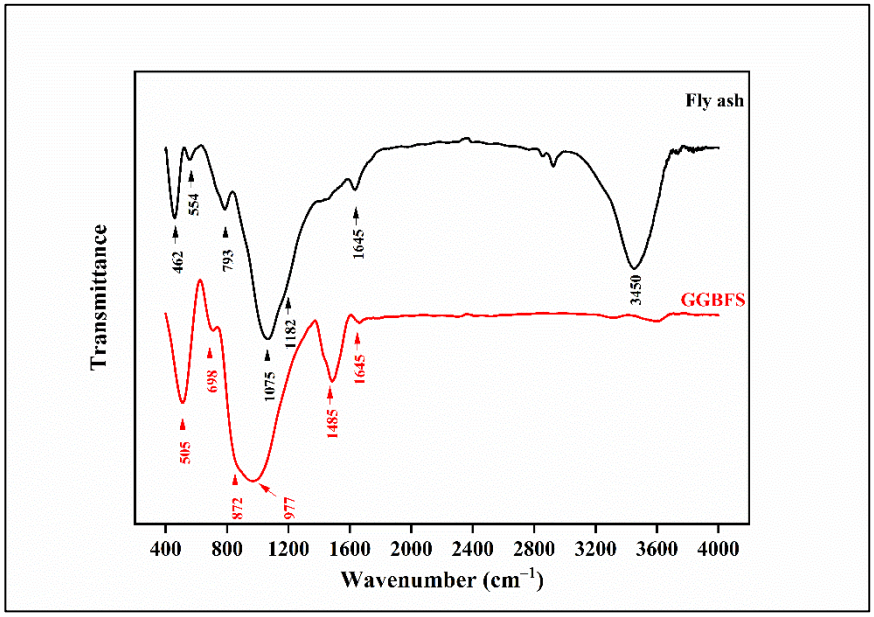

Figure A.2. FTIR spectra of powders.

949

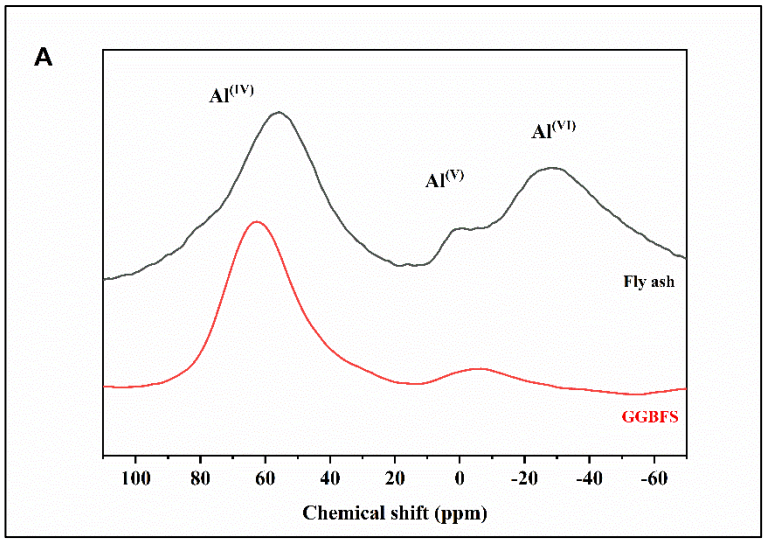

950

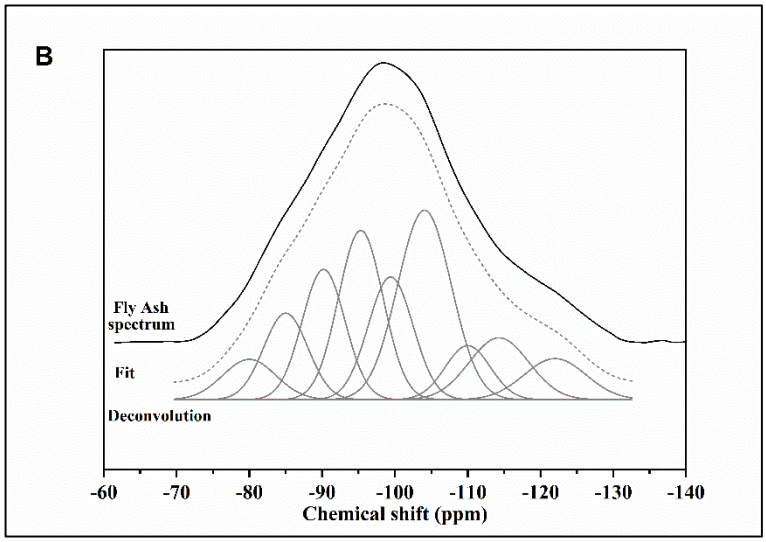

951

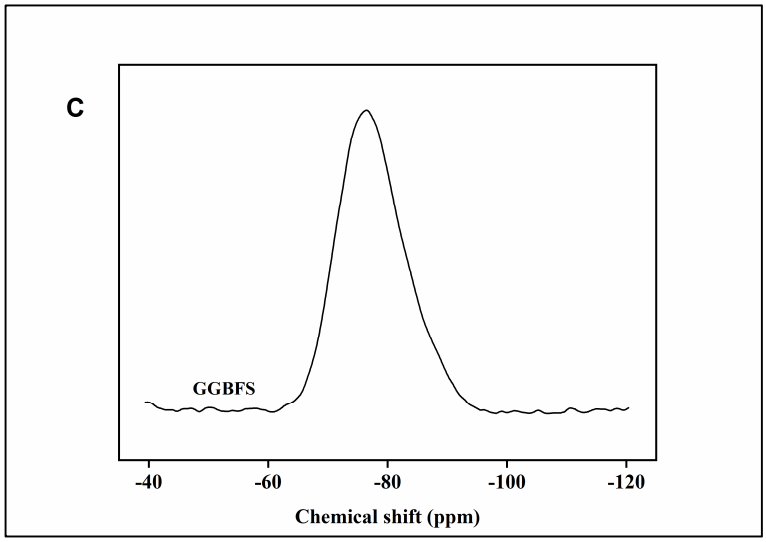

952 Figure A.3. ^{27}Al (A) and ^{29}Si MAS NMR of powders (B: Fly ash, C: GGBFS).

953

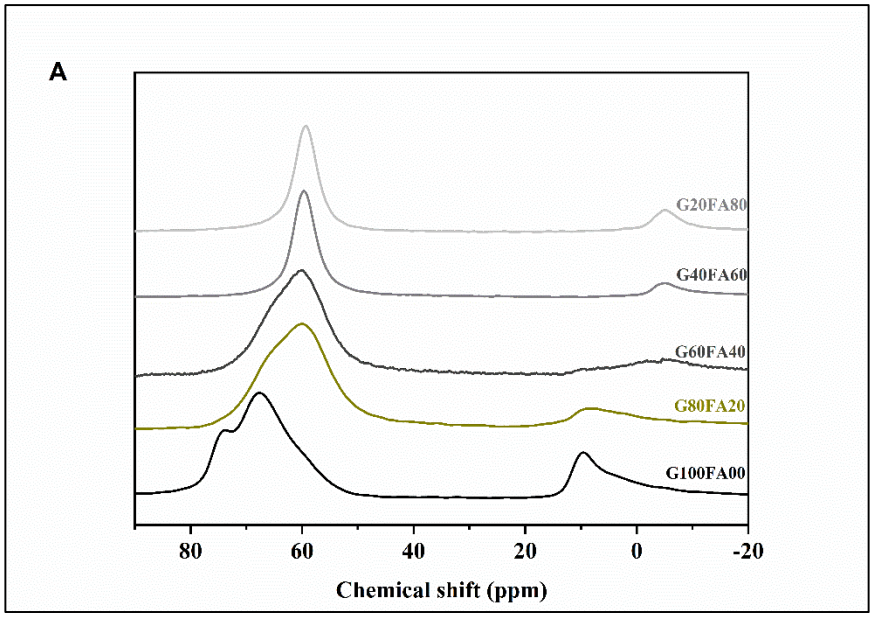

954

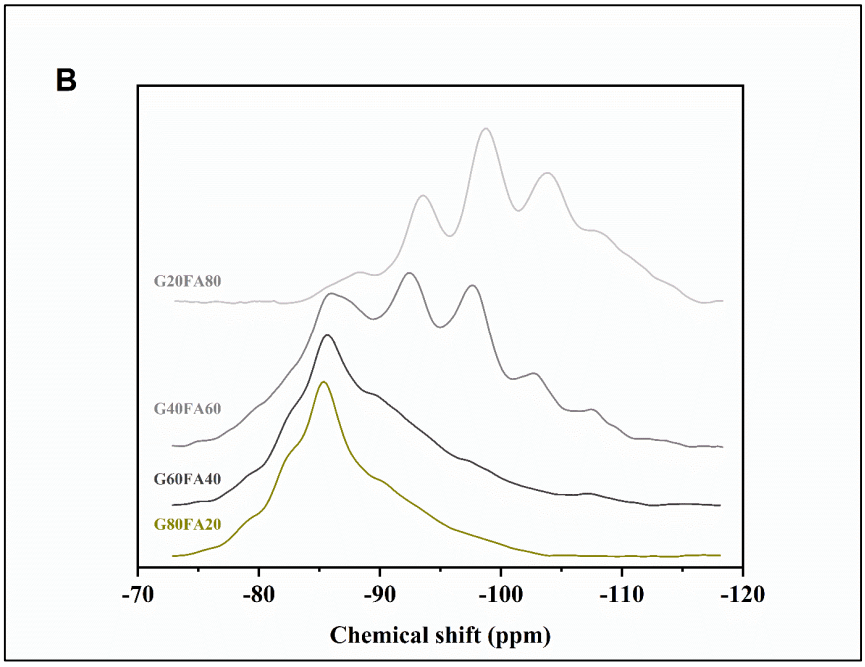

955

956 Figure A.4 ^{27}Al (A) and ^{29}Si (B) MAS NMR of slag-fly ash grouts.

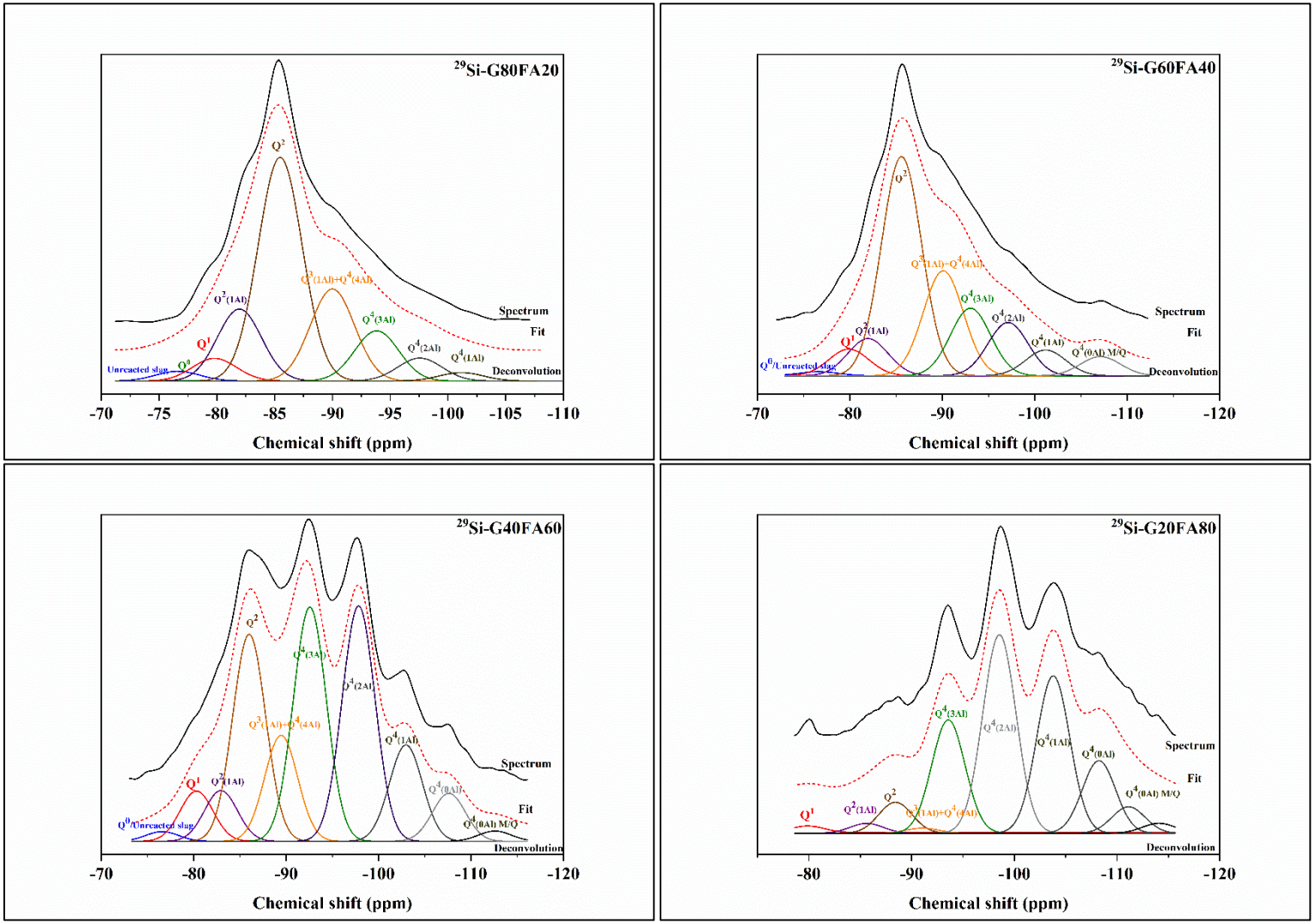

Figure A.5. Deconvoluted ^{29}Si MAS NMR spectra of alkali activated slag-fly ash blends.

Table A.1. Deconvolution results of ^{29}Si MAS NMR alkali activated slag-fly ash blends

G100 FA00		**Unreacted slag**	**Q^0**	**Q^1_{a-b}**	**Q^2(1Al)**	**Q^2_{b-p}**	**Q^3(1Al)/Q^4(4Al)**	**Q^4(3Al)**					
	xc	-76.3	-76.1	78	-82	-86.1	-89.7	-92.3					
	A	0.14	0.01	0.81	1.81	2.75	0.33	0.22					
	w	2.37	2.37	2.37	2.37	2.37	2.37	2.37					
	%	2.26	0.32	13.11	29.88	45.45	5.41	3.55					
G80 FA20		**Unreacted slag**	**Q^0**	**Q^1_{a-b}**	**Q^2(1Al)**	**Q^2_{b-p}**	**Q^3(1Al)/Q^4(4Al)**	**Q^4(3Al)**	**Q^4(2Al)**	**Q^4(1Al)**			
	xc	-76,61	-76.10	-79.80	-81.95	-85.48	-90.00	-93.83	-97.57	-101.17			
	A	0.18	0.01	0.42	1.32	4.10	1.69	0.92	0.42	0.15			
	w	4.50	4.50	4.50	4.50	4.50	4.50	4.50	4.50	4.50			
	%	1.94	0.09	4.52	14.33	44.54	18.32	9.99	4.57	1.68			
G60 FA40		**Q^0/Unreacted slag**		**Q^1_{a-b}**	**Q^2(1Al)**	**Q^2_{b-p}**	**Q^3(1Al)/Q^4(4Al)**	**Q^4(3Al)**	**Q^4(2Al)**	**Q^4(1Al)**	**Q^4(0Al)**	**$Q^4(0Al)_{M/Q}$**	
	xc	-76.61		-79.88	-81.95	-85.58	-90.10	-93.04	-97.10	-101.17	-107.10		
	A	0.09		0.55	0.77	4.55	2.18	1.40	1.11	0.53	0.40		
	w	5.10		5.10	5.10	5.10	5.10	5.10	5.10	5.10	5.10		
	%	0.74		4.79	6.67	39.28	18.81	12.11	9.55	4.61	3.44		
G40 FA60		**Q^0/Unreacted slag**		**Q^1_{a-b}**	**Q^2(1Al)**	**Q^2_{b-p}**	**Q^3(1Al)/Q^4(4Al)**	**Q^4(3Al)**	**Q^4(2Al)**	**Q^4(1Al)**	**Q^4(0Al)**	**$Q^4(0Al)_{M/Q}$**	
	xc	-76.58		-80.30	-82.95	-86.00	-89.46	-92.56	-97.83	-102.95	-107.61	-112.59	
	A	0.17		0.86	0.87	3.54	1.81	4.00	4.03	1.65	0.82	0.18	
	w	4.20		4.20	4.20	4.20	4.20	4.20	4.20	4.20	4.20	4.20	4.20
	%	0.93		4.80	4.84	19.76	10.11	20.01	22.47	9.20	4.58	2.98	
G20 FA80				**Q^1_{a-b}**	**Q^2(1Al)**	**Q^2_{b-p}**	**Q^3(1Al)/Q^4(4Al)**	**Q^4(3Al)**	**Q^4(2Al)**	**Q^4(1Al)**	**Q^4(0Al)**	**$Q^4(0Al)_{M/Q}$**	
	xc			-79.87	-85.63	-88.43	-91.05	-93.58	-98.55	-103.79	-108.24	-111.13	-114.09
	A			0.12	0.19	0.59	0.10	2.16	3.78	3.00	1.38	0.50	0.19
	w			3.80	3.80	3.80	3.80	3.80	3.80	3.80	3.80	3.80	3.80
	%			1.04	1.56	4.92	0.81	17.96	31.46	24.96	11.51	4.20	1.58